

Relationship between SDOF-Input-Energy and Fourier Amplitude Spectral Amplification Ratios

Haizhong Zhang¹, Yan-Gang Zhao^{*2}, Tsutomu Ochiai¹, and Yingchi Fang¹

ABSTRACT

This article presents the theoretical relationship between the site amplification ratio of the input energy spectrum for a single-degree-of-freedom system (SDOF) and that of the Fourier amplitude spectrum (FAS). The relationship indicates that the input energy spectral ratio is the result of smoothing the square of the Fourier amplitude spectral ratio. The spectral window for smoothing is determined by the bedrock-motion FAS and the oscillator transfer function for the relative velocity. The characteristics of the input energy spectral ratio were derived based on the idea of smoothing and confirmed based on real seismic records. The findings of this study contribute to a better understanding of site effects on the input energy spectrum.

KEY POINTS

- This article shows a relationship between single-degree-of-freedom (SDOF)-input-energy and Fourier amplitude spectral amplification ratios.
- The input energy spectral ratio is the result of smoothing the square of the Fourier amplitude spectral ratio.
- The spectral window for smoothing is determined by the bedrock motion and the oscillator transfer function.

INTRODUCTION

Since the fundamental work by Housner (1956), a number of extensive studies (Zahrah and Hall, 1984; Akiyama, 1985; Kuwamura and Galambos, 1989; Decanini and Mollaioli, 1998, 2001) have been conducted to promote energy-based seismic design. In contrast to the conventional force- or displacement-based seismic designs that focus only on the maximum force or deformation, energy-based design considers the effects of cumulative damage caused by cyclic inelastic responses. Because potential structural damage is more highly correlated with cumulative damage than a simple peak response (Erberik and Sucuoglu, 2004; Benavent-Climent, 2007; Acun and Sucuoglu, 2010), energy-based seismic design has become increasingly popular in recent decades. The goal of energy-based seismic design is to ensure that the energy dissipation capacity of a structure exceeds the imparted earthquake energy into the structure. Therefore, it is necessary to determine the imparted earthquake energy into a structure before conducting an energy-based seismic design.

The input energy spectrum has been widely used to characterize the imparted earthquake energy into a structure, because it is a stable quantity determined primarily by the structural mass

and natural period, and it is typically uncoupled with the energy dissipation capacity of the structure. Although the hysteretic energy spectrum instead of the input energy spectrum is directly used for energy-based seismic design, many studies prefer to first determine the input energy spectrum and then obtain the hysteretic energy spectrum based on a hysteretic-to-input energy ratio spectrum. The input energy spectrum is always expressed in the form of the energy equivalent velocity spectrum to eliminate the effect of the structural mass. Numerous studies have been devoted to the development of the input energy spectrum for energy-based seismic design. Kuwamura and Galambos (1989), Akiyama *et al.* (1993), Decanini and Mollaioli (1998, 2001), Kunnath and Chai (2004), Vahdani *et al.* (2019), and Zhang *et al.* (2023) discussed the overall methodology for the determination of the input energy spectral design model. Chai and Fajfar (2000), Riddell and Garcia (2001), Benavent-Climent *et al.* (2002, 2010), Amiri *et al.* (2008), López-Almansa *et al.* (2013), Dindar *et al.* (2015), and Mezgebo and Lui (2016) discussed the spectral shapes and normalization factors suitable for the construction of design input energy spectrum. The shape of the energy equivalent velocity spectrum, V_E , is found to be similar to that of the velocity response spectrum; V_E increases from zero to maximum and nearly keeps constant with the increasing period for large magnitude earthquakes but falls off with the period for moderate-to-small magnitude earthquakes. Therefore, bilinear and three-

1. Department of Architecture, Kanagawa University, Yokohama, Kanagawa, Japan;

2. Key Laboratory of Urban Security and Disaster Engineering of Ministry of Education, Beijing University of Technology, Beijing, China

*Corresponding author: zhao@kanagawa-u.ac.jp

Cite this article as Zhang, H., Y.-G. Zhao, T. Ochiai, and Y. Fang (2023).

Relationship between SDOF-Input-Energy and Fourier Amplitude Spectral Amplification Ratios, *Bull. Seismol. Soc. Am.* **XX**, 1–18, doi: [10.1785/0120220154](https://doi.org/10.1785/0120220154)

© Seismological Society of America

piece forms are always used to model the V_E for seismic design. Chapman (1999), Chou and Uang (2000), Gong and Xie (2005), Cheng *et al.* (2014, 2020), and Alici and Sucuoğlu (2016, 2018), explored the attenuation model of the input energy spectrum. They found that the input energy spectrum cannot only be affected by the well-known magnitude and site-to-source distance but also by fault mechanisms. Thus, they developed attenuation models incorporating these parameters based on different earthquake databases. Most of these studies also discussed the effect of the local site on the input energy spectrum based on statistical analyses of seismic ground motions, and almost all of them found that the input energy spectrum can be significantly affected by local site conditions irrespective of the spectral shape or attenuation model. Furthermore, the input energy spectrum on soft soil was found to be typically larger than that on stiff sites, and this trend is more prominent for the long-period band. However, theoretical discussions regarding site effects on the input energy spectrum have never been systematically conducted.

This study presents a theoretical relationship between the site amplification ratio of the input energy spectrum for a single-degree-of-freedom (SDOF) and that of the Fourier amplitude spectrum (FAS), thereby generating a better theoretical understanding of site effects on the input energy spectrum. The remainder of this article is organized as follows. First, a theoretical relationship between the input energy spectral ratio (IESR) and the Fourier amplitude spectral ratio (FASR) was derived. Then, the derived relationship was verified based on real seismic records and site response analyses. Subsequently, the characteristics of the IESR were comprehensively explored and explained based on the derived relationship and were compared to those of the FASR as well as response spectral ratios. Thereafter, the statistical supports for the theoretically derived characteristics of the IESR based on real seismic ground motions recorded on nearby soil-rock pairs were presented. Finally, the conclusions were drawn.

THEORETICAL RELATIONSHIP BETWEEN THE IESR AND THE FASR

Consider an SDOF subjected to a ground acceleration \ddot{x}_g ; the dynamic equation of the SDOF can be written as:

$$m\ddot{x} + c\dot{x} + f_s = -m\ddot{x}_g, \quad (1)$$

in which m is the mass, c is the damping coefficient, f_s is the restoring force, and x is the relative displacement. Then, the energy balance equation can be derived by integrating equation (1) with respect to x :

$$E_k + E_\xi + E_s = E_I, \quad (2)$$

in which, $E_k = \int_0^t m\dot{x} \dot{x} dt$ is the kinetic energy, $E_\xi = \int_0^t c\dot{x}^2 dt$ is the energy dissipated via damping, $E_s = \int_0^t f_s \dot{x} dt$ is the

energy absorbed by the spring, and $E_I = \int_0^t -m\ddot{x}_g \dot{x} dt$ is the total input energy delivered by the earthquake (referred to as the input energy spectrum in this study). To eliminate the dependence on mass, the input energy spectrum E_I can be converted into the energy equivalent velocity spectrum, V_E , via the following expression:

$$V_E = \sqrt{\frac{2E_I}{m}}. \quad (3)$$

Kuwamura *et al.* (1994) and Ordaz *et al.* (2003) discussed the theoretical relationship between the input energy spectrum E_I and the acceleration FAS (denoted by $F(\omega)$), and Ordaz *et al.* (2003) provided a theoretical relationship in the form:

$$\frac{E_I(\bar{\omega}, \xi)}{m} = \frac{-1}{\pi} \int_0^\infty |F(\omega)|^2 \text{Re}[Hv(\bar{\omega}, \omega, \xi)] d\omega, \quad (4)$$

in which ω is the circular frequency of the FAS, $\bar{\omega}$ is the circular frequency of the SDOF, and ξ is the oscillator damping ratio. Here, it should be noted that the circular frequency ω of the FAS is different from the oscillator circular frequency $\bar{\omega}$. $Hv(\bar{\omega}, \omega, \xi)$ is the oscillator transfer function of the relative velocity with respect to the ground acceleration, which is a complex number. Its real part can be expressed as:

$$\text{Re}[Hv(\bar{\omega}, \omega, \xi)] = \frac{-2\xi\bar{\omega}\omega^2}{(\bar{\omega}^2 - \omega^2)^2 + (2\xi\bar{\omega}\omega)^2}. \quad (5)$$

Equation (4) is crucial for establishing the relationship between the input energy spectrum and the FAS. The principle of calculating the input energy spectrum from the input FAS is different from that of calculating the traditional oscillator response FAS. It is known that the oscillator response FAS is expressed as the product of the input FAS and oscillator transfer function, whereas the input energy spectrum is expressed in the form of integration related to the input FAS and the oscillator transfer function. In addition, the absolute value of the oscillator transfer function is used for the calculation of the oscillator response FAS, whereas the real part of the oscillator transfer function (relative velocity with respect to ground acceleration) is used for the calculation of the input energy spectrum.

According to equation (4), the input energy spectrum of a seismic motion on a reference outcrop bedrock, E_{IB} , can be expressed as:

$$\frac{E_{IB}(\bar{\omega}, \xi)}{m} = \frac{1}{\pi} \int_0^\infty |F_B(\omega)|^2 (-\text{Re}[Hv(\bar{\omega}, \omega, \xi)]) d\omega, \quad (6)$$

in which $F_B(\omega)$ is the FAS of the seismic motion at the outcrop bedrock. Then, considering a soil site on the bedrock, the input

energy spectrum of the ground-surface motion transmitted from the bedrock, E_{IS} , is obtained as:

$$\frac{E_{IS}(\bar{\omega}, \xi)}{m} = \frac{1}{\pi} \int_0^{\infty} |F_S(\omega)|^2 (-\text{Re}[Hv(\bar{\omega}, \omega, \xi)]) d\omega. \quad (7)$$

Here, $F_S(\omega)$ is the FAS of the ground-surface motion of the soil site, which is related to the FAS of the incident bedrock motion $F_B(\omega)$ via

$$F_S(\omega) = |Tr(\omega)|F_B(\omega), \quad (8)$$

in which $|Tr(\omega)|$ is the modular of the site transfer function, that is, the Fourier amplitude spectral ratio (FASR), which is the well-understood tool for characterizing site effects. In this study, $Tr(\omega)$ is assumed to be the site transfer function attributed to vertically propagating shear waves. Using such an assumption can simply reflect the primary characteristics of site amplification, although it may not be applicable for all sites, for example, those inside large basins in which surface waves may be induced (Kawase, 2003; Nakano and Kawase, 2019).

Subsequently, the ratio of the input energy spectrum at the ground surface to that on the outcrop bedrock can be derived by combining equations (6–8):

$$\frac{E_{IS}(\bar{\omega}, \xi)}{E_{IB}(\bar{\omega}, \xi)} = \frac{\int_0^{\infty} |F_B(\omega)|^2 (-\text{Re}[Hv(\bar{\omega}, \omega, \xi)]) |Tr(\omega)|^2 d\omega}{\int_0^{\infty} |F_B(\omega)|^2 (-\text{Re}[Hv(\bar{\omega}, \omega, \xi)]) d\omega}. \quad (9)$$

For convenience, equation (9) is rearranged as:

$$\frac{E_{IS}(\bar{\omega}, \xi)}{E_{IB}(\bar{\omega}, \xi)} = \int_0^{\infty} U_e(\bar{\omega}, \omega, \xi) |Tr(\omega)|^2 d\omega, \quad (10)$$

$$U_e(\bar{\omega}, \omega, \xi) = \frac{W_e(\bar{\omega}, \omega, \xi)}{\int_0^{\infty} W_e(\bar{\omega}, \omega, \xi) d\omega}, \quad (11)$$

in which $W_e(\bar{\omega}, \omega, \xi)$ is determined by the FAS of the bedrock motion and the oscillator transfer function for the relative velocity $Hv(\bar{\omega}, \omega, \xi)$ and is expressed as:

$$W_e(\bar{\omega}, \omega, \xi) = |F_B(\omega)|^2 (-\text{Re}[Hv(\bar{\omega}, \omega, \xi)]). \quad (12)$$

Equation (10) relates the IESR (E_{IS}/E_{IB}) and FASR ($|Tr(\omega)|$). Based on equation (10), site effects on the input energy spectra can be systematically explored, as detailed subsequently.

By further considering the relationship between the input energy spectrum and the energy equivalent velocity spectrum expressed by equation (3), the ratio of the energy equivalent velocity spectrum at the ground surface V_{ES} to that on the outcrop bedrock V_{EB} , that is, V_{ES}/V_{EB} , can be expressed as:

$$\left(\frac{V_{ES}(\bar{\omega}, \xi)}{V_{EB}(\bar{\omega}, \xi)} \right)^2 = \int_0^{\infty} U_e(\bar{\omega}, \omega, \xi) |Tr(\omega)|^2 d\omega. \quad (13)$$

VERIFICATION OF THE DERIVED RELATIONSHIP

To validate the derived relationship, two seismic ground motions recorded on a pair of adjacent engineering rock and soil sites were selected from strong-motion seismograph networks, Kyoshin net (K-NET), Kiban–Kyoshin network (KiK-net; Okada *et al.*, 2004; Aoi *et al.*, 2011), which were constructed by the National Research Institute for Earth Science and Disaster Prevention (NIED) (2019). In this study, the engineering bedrock is defined with surface-layer shear-wave velocity being greater than 400 m/s, according to the Japanese Seismic Design Code (2000). The definition of the engineering bedrock may vary greatly in different countries, the shear-wave velocity for the engineering bedrock defined in the Japanese Seismic Design Code (2000) is much smaller than that in the National Earthquake Hazards Reduction Program (NEHRP) (2000). The two ground motions were taken from the same earthquake, which had a Japan Meteorological Agency magnitude M_{JMA} of 6.1 and epicentral distance R_e of 241 km. The two ground motions on engineering rock and soil sites are both east–west horizontal components. The rock and soil sites are 4.1 km away, which may not be close enough to eliminate the possible local topographic effect, although we searched all sites in K-NET and KiK-net to find the ideal site pairs. The shear-wave velocity (V_S) profiles of the two sites are shown in Figure 1. The rock and soil sites were coded as AOMH03 and AOM006, and their altitudes are 20 m and 2 m, respectively.

Then, the ratio V_{ES}/V_{EB} was directly calculated using the two seismic records of the soil and rock sites according to the definitions in equations (2) and (3). Two values of the oscillator damping ratio ξ : 5% and 10%, are considered, because both are always used in the definition of the input energy spectrum for seismic design (Akiyama *et al.*, 1993; Chai and Fajfar, 2000; López-Almansa *et al.*, 2013; Dindar *et al.*, 2015). The obtained V_{ES}/V_{EB} values were compared to those calculated from the FASR using the proposed relationship (equation 13), as shown in Figure 2a,b. The FASR was calculated as the FAS ratio of the ground motion on the soil site to that on the rock site. Here, the surface layer of the rock site (AOMH03) is considered to be the engineering bedrock for the soil site (AOM006), and the bedrock motion acts as the input for the soil site. In addition, the amplification ratios between the soil to rock sites are considered to be mainly attributed to vertically propagated shear waves, and the possible basin-induced surface waves (Kawase, 2003; Nakano and Kawase, 2019), as well as topographic effects, are ignored. It is evident from Figure 2a,b that the V_{ES}/V_{EB} results obtained by the proposed relationship totally agree with those based on real seismic records.

In addition, the derived relationship was further verified based on site response analyses. To this end, another actual site, coded as TCGH16, was selected from the KiK-net. The shear-wave velocity profile of the site is shown in Figure 1, and the bedrock level is indicated by the arrow. The soil

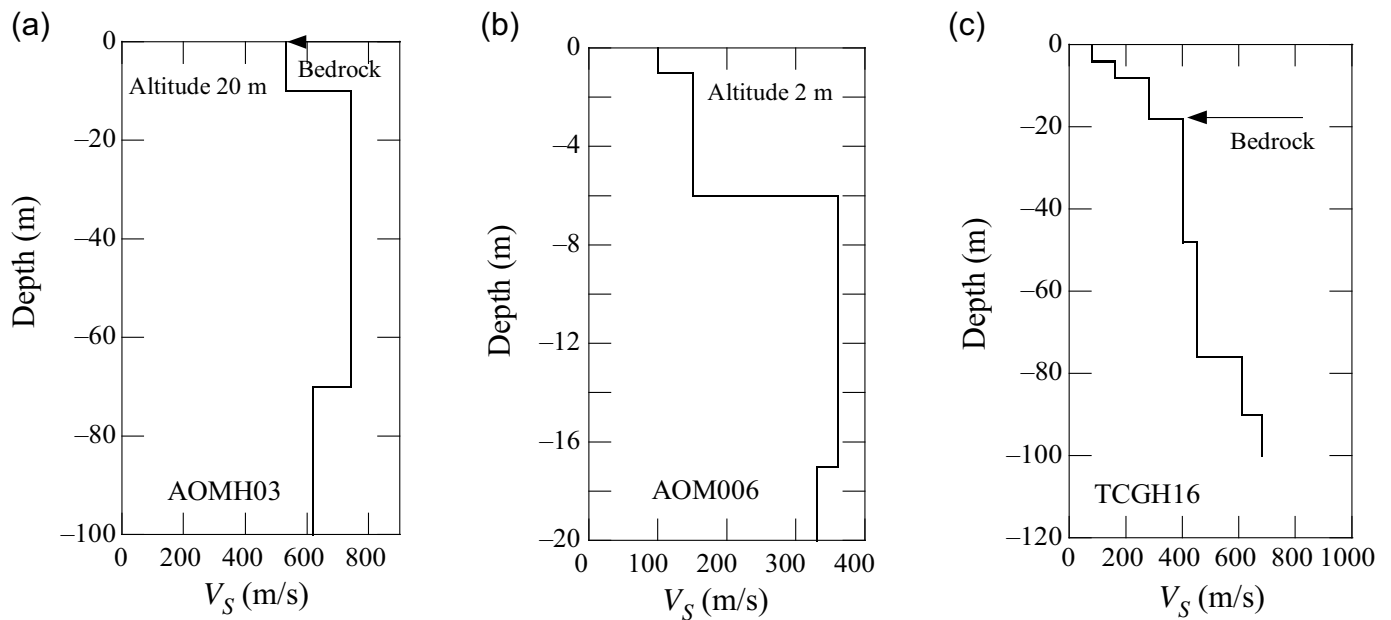


Figure 1. Shear-wave velocity V_S profiles of the three actual sites in Japan used for the verification: (a) site AOMH03; (b) site AOM006; (c) site TCGH16.

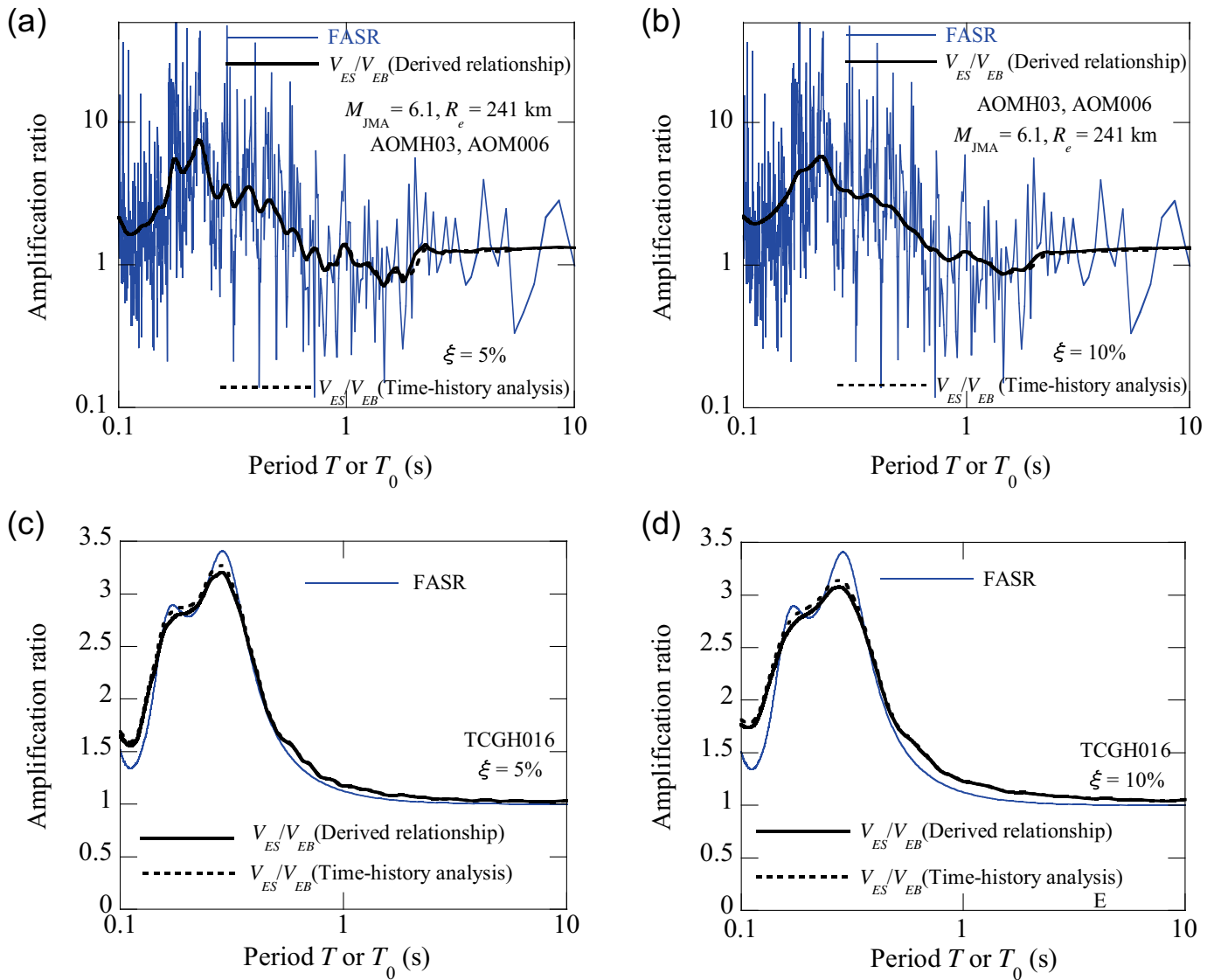
damping ratio was simply set to 2.5% for linear analysis, although it may be more complex for real cases depending on the shear-wave velocity and the depth of the soil layer (Kokusho, 2017). The incident motion on the outcrop bedrock used for the analysis was generated from the design response spectrum specified on the bedrock corresponding to the damage limit state in the Japanese Seismic Design Code (2000), using the commercial software SNAP-WAVE (Kozo System, Inc., unpublished report; see Data and Resources). The generated artificial wave has a long tail at the end to allow the free ground vibration to be close to zero. The principle underlying the generation of the artificial wave involves iteratively adjusting a FAS until the response spectrum of the generated wave becomes equal to the target spectrum within a certain margin of error. The initial FAS is approximated from the zero-damped velocity response spectrum, which is constructed based on the target spectrum. In addition, a random phase is adopted for generating the artificial wave. To ensure that the displacement of the generated wave is reasonable, a high-pass filter with a corner frequency of 0.1 Hz (10 s) was adopted to process the generated wave, and the processed wave is shown in Figure 3.

Then, applying equation (13), V_{ES}/V_{EB} was calculated from the FASR that was directly obtained using the SHAKE program (Idriss and Sun, 1992). The obtained V_{ES}/V_{EB} values using equation (13) were compared to those directly calculated using the time-history accelerations at the ground surface and bedrock as shown in Figure 2c,d. The time-history acceleration on the ground surface was obtained from that on the bedrock through site-response analysis using the SHAKE program (Idriss and Sun, 1992). It is evident from Figure 2c,d that the results of the proposed relationship totally agree with those based on the site response analyses. It should be noted that the horizontal ordinates for V_{ES}/V_{EB} and the FASR are different,

although they are represented by the same axis in Figure 2. The horizontal ordinate for the FASR is the period of the FAST ($T = 2\pi/\omega$), and that for V_{ES}/V_{EB} is the oscillator period T_0 ($T_0 = 2\pi/\bar{\omega}$). In addition, it can be observed from Figure 2 that V_{ES}/V_{EB} slightly becomes smoother with increasing oscillator damping ratio ξ .

PROPERTIES OF THE IESR BASED ON THE DERIVED RELATIONSHIP

This section explores the properties of the IESR based on the derived relationship expressed by equation (10). It is found that equation (10) essentially represents the procedure for smoothing a function. $|Tr(\omega)|^2$ is the function to be smoothed, $U_e(\bar{\omega}, \omega, \xi)$ is the spectral window for smoothing, and E_{IS}/E_{IB} is the result obtained after smoothing. The term $U_e(\bar{\omega}, \omega, \xi)$ satisfies the condition required for the spectral window for smoothing (i.e., $\int_0^{+\infty} U_e(\bar{\omega}, \omega, \xi) d\omega = 1$). Figure 4 illustrates the smoothing process as represented by equation (10). The smoothing process at each oscillator period T_0 involves a weighted average calculation and the spectral window for smoothing acts as the weight function. Specifically, the value of the IESR at an oscillator period T_0 is equal to the weighted average of the $|Tr(\omega)|^2$ values at circular frequencies ω from zero to infinity, and the value of $U_e(\bar{\omega}, \omega, \xi)$ at the circular frequency ω is the weight for the $|Tr(\omega)|^2$ value at the same circular frequency. To calculate the values of the IESR at different oscillator periods, the smooth window $U_e(\bar{\omega}, \omega, \xi)$ needs to be shifted to the target oscillator period T_0 . The smoothing process as represented by equation (10) can be preliminarily understood by comparing the overall shapes of V_{ES}/V_{EB} and the FASR $|Tr(\omega)|$ shown in Figure 2.



Spectral window for smoothing

To clarify the properties of the IESR based on the idea of smoothing, the characteristics of the spectral window for smoothing $U_e(\bar{\omega}, \omega, \xi)$ are investigated. It is evident from equations (11) and (12) that $U_e(\bar{\omega}, \omega, \xi)$ is determined by the bedrock-motion FAS $F_B(\omega)$ and the real part of the oscillator transfer function $Re[Hv(\bar{\omega}, \omega, \xi)]$. The representative results of $-Re[Hv(\bar{\omega}, \omega, \xi)]$ and $|F_B(\omega)|^2$ are presented in Figures 5 and 6, respectively, to illustrate their properties. In Figure 5, three oscillator periods ($T_0 = 0.1, 0.5,$ and 2 s) are considered, and the oscillator damping ratio ξ was set to 5%. In Figure 6, the bedrock-motion FAS $F_B(\omega)$ was generated based on a widely used FAS model introduced by Boore (2003). This FAS model incorporates the effects of the source, path, and site characteristics (Zhang and Zhao, 2020, 2021b,c). Three values of the moment magnitude ($M = 4, 6,$ and 8) were considered, and the site-to-source distance R of 20 km was chosen. The seismological parameters necessary for the determination of $F_B(\omega)$, for example, the stress drop $\Delta\sigma$ (bar), site diminution

Figure 2. Comparison between the amplification ratios of the energy equivalent velocity spectra, that is, velocity spectrum at the ground surface to that on the outcrop bedrock (V_{ES}/V_{EB}), calculated by the derived relationship and those obtained from (a,b) real seismic records and (c,d) site response analyses. The color version of this figure is available only in the electronic edition.

κ_0 (s), mass density of the crust ρ (g/cm^3), shear-wave velocity of the crust β (km/s), geometrical attenuation $Z(R)$, anelastic attenuation $Q(f)$, and crustal amplification $A(f)$, were determined based on the study by Boore and Thompson (2015), as summarized in table 1 of Wang and Rathje (2016).

Figure 5 shows that irrespective of the shift of the oscillator period T_0 , $-Re[Hv(\bar{\omega}, \omega, 5\%)]$ has a very sharp peak around T_0 (i.e., $T \approx T_0$), and the values of $-Re[Hv(\bar{\omega}, \omega, 5\%)]$ decrease rapidly toward zero as the period T deviates from T_0 . In addition, the peak value of $-Re[Hv(\bar{\omega}, \omega, 5\%)]$ increases with increasing oscillator period T_0 . This can be understood based on the expression for the peak value, which can be obtained as

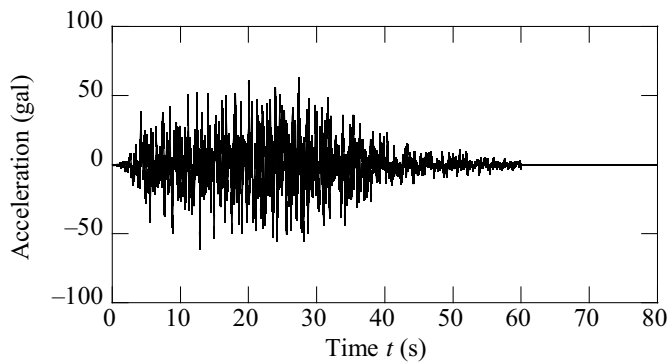


Figure 3. Seismic wave generated from the design response spectrum specified on the bedrock corresponding to the damage limit state in the Japanese Seismic Design Code (2000).

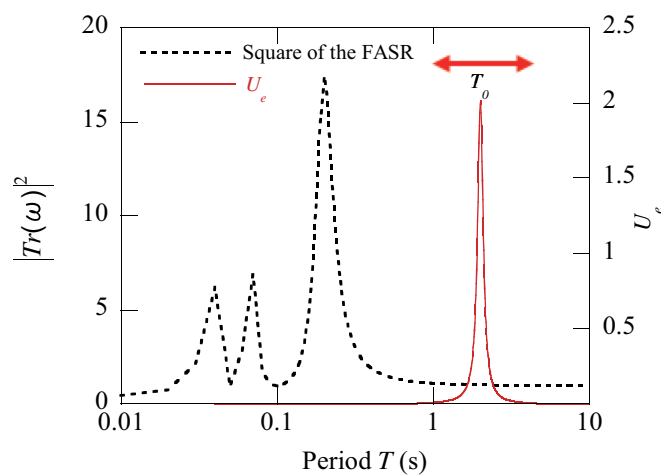


Figure 4. Illustration of the smoothing process represented by equation (10). The color version of this figure is available only in the electronic edition.

$T_0/4\pi\xi$ by setting $\omega = \bar{\omega}$ in equation (5). Figure 6 shows that the overall shape of $|F_B(\omega)|^2$ is much flatter compared with that of $-Re[Hv(\bar{\omega}, \omega, 5\%)]$ and changes with the moment magnitude. When the moment magnitude is small ($M = 4$), $|F_B(\omega)|^2$ exhibits an obvious peak in a short period. As the moment magnitude increases, the long-period components of $|F_B(\omega)|^2$ increase relative to the short-period components, the peak becomes less obvious, and the overall shape of $|F_B(\omega)|^2$ becomes flatter.

According to the properties of $|F_B(\omega)|^2$ and $-Re[Hv(\bar{\omega}, \omega, 5\%)]$, the characteristics of $U_e(\bar{\omega}, \omega, 5\%)$ can be understood. As indicated by equations (11) and (12), $U_e(\bar{\omega}, \omega, 5\%)$ is expressed in the form of the product of $|F_B(\omega)|^2$ and $-Re[Hv(\bar{\omega}, \omega, 5\%)]$, and the shape of $U_e(\bar{\omega}, \omega, 5\%)$ is determined by those of $-Re[Hv(\bar{\omega}, \omega, 5\%)]$ and $|F_B(\omega)|^2$. Because $-Re[Hv(\bar{\omega}, \omega, 5\%)]$ has a very sharp peak around the oscillator period T_0 and the overall shape of $|F_B(\omega)|^2$ is much flatter than that of $-Re[Hv(\bar{\omega}, \omega, 5\%)]$,

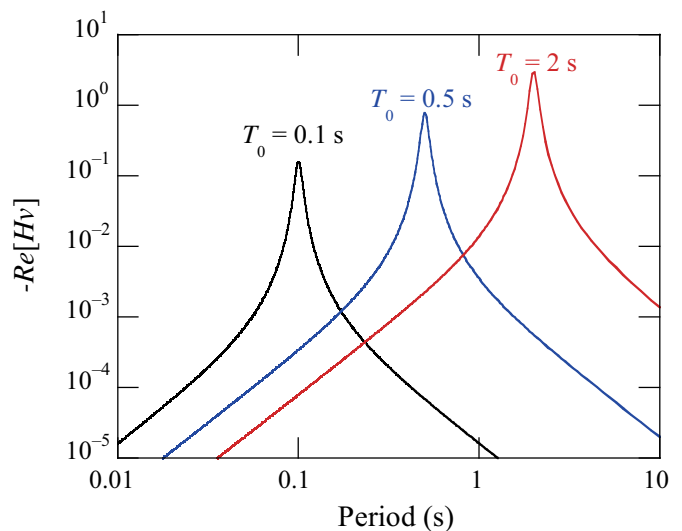


Figure 5. Values related to the real part of the oscillator transfer function for the relative velocity $-Re[Hv(\bar{\omega}, \omega, 5\%)]$ for three different oscillator periods. The color version of this figure is available only in the electronic edition.

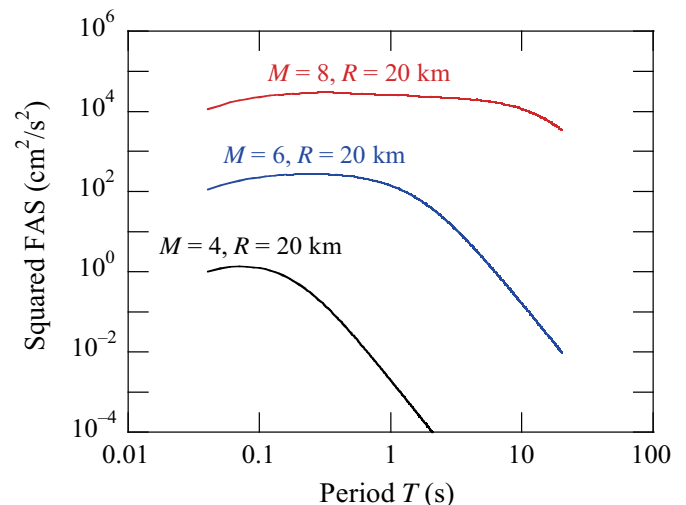
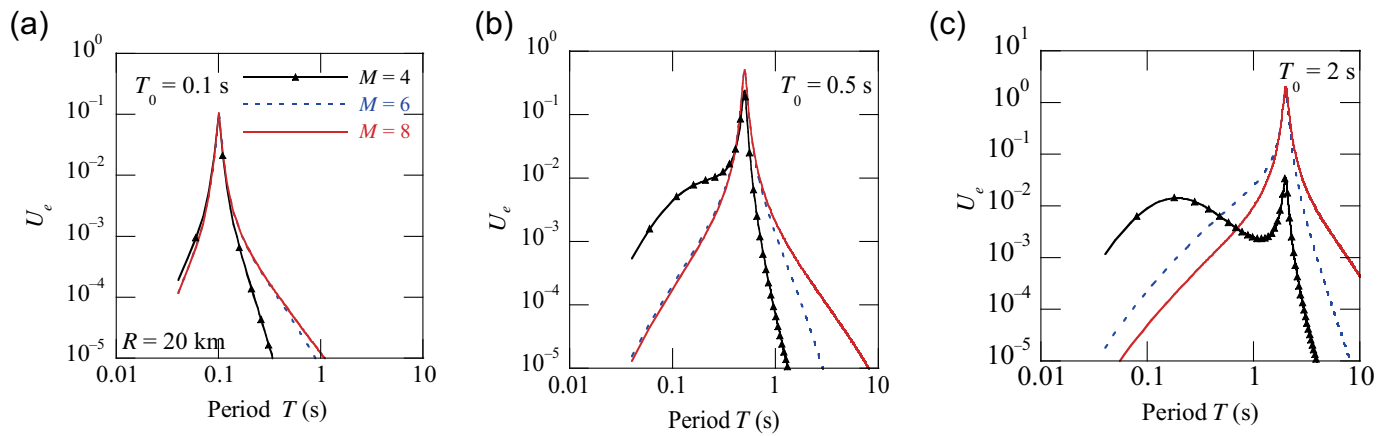


Figure 6. Squared values of the bedrock-motion Fourier amplitude spectra (FAS) $F_B(\omega)$ for three different values of the moment magnitude M . The color version of this figure is available only in the electronic edition.

$U_e(\bar{\omega}, \omega, 5\%)$ typically has a sharp peak around the oscillator period T_0 . This property can be supported by Figure 7, which presents the results of $U_e(\bar{\omega}, \omega, 5\%)$ for various bedrock motions and oscillator periods. This means that the weights of the spectral window are typically concentrated around the oscillator period T_0 .

In addition, because $|F_B(\omega)|^2$ varies with the moment magnitude, $U_e(\bar{\omega}, \omega, 5\%)$ also changes with the moment magnitude. Because the long-period components of $|F_B(\omega)|^2$ increase relative to the short-period components as the moment magnitude increases, $U_e(\bar{\omega}, \omega, 5\%)$ should have the same trend. This



property can be demonstrated by comparing the results of $U_e(\bar{\omega}, \omega, 5\%)$ with different values of the moment magnitude in Figure 7. This means that the weights of the smooth window shift to long periods, as the moment magnitude increases.

Moreover, the dependency of $U_e(\bar{\omega}, \omega, 5\%)$ on the moment magnitude changes with the oscillator period T_0 . Figure 7 shows that $U_e(\bar{\omega}, \omega, 5\%)$ is more dependent on the moment magnitude at long oscillator periods (Fig. 7c) than at short oscillator periods (Fig. 7a). The reason can be primarily attributed to the relative positions of the peaks of $-Re[Hv(\bar{\omega}, \omega, 5\%)]$ and $|F_B(\omega)|^2$. When the moment magnitude is small, $|F_B(\omega)|^2$ exhibits an obvious peak in a short period, as shown in Figure 6. If the peak of $-Re[Hv(\bar{\omega}, \omega, 5\%)]$ is far enough from the peak of $|F_B(\omega)|^2$ (i.e., the oscillator period is sufficiently long), two peaks may occur in $U_e(\bar{\omega}, \omega, 5\%)$, in which one peak is around the oscillator period T_0 , and the other is around the predominant period of $|F_B(\omega)|^2$, as shown in Figure 7c. As the moment magnitude increases, because the peak of $|F_B(\omega)|^2$ becomes less obvious and the overall shape becomes flatter, the peak around the predominant period of $|F_B(\omega)|^2$ disappears in $U_e(\bar{\omega}, \omega, 5\%)$. However, when the peak of $-Re[Hv(\bar{\omega}, \omega, 5\%)]$ is close to that of $|F_B(\omega)|^2$ (i.e., the oscillator period is short), only one peak occurs in $U_e(\bar{\omega}, \omega, 5\%)$ (Fig. 7a) regardless of the moment magnitude. Therefore, $U_e(\bar{\omega}, \omega, 5\%)$ varies more significantly with the moment magnitude in long oscillator periods than in short oscillator periods. This also means that when the oscillator period is long, the weights of the smoothing window scatter around the oscillator period and the fundamental period of the FAS for a small moment magnitude; however, they shift to the oscillator period T_0 with increasing moment magnitude as shown in Figure 7c.

Properties of the IESR

Based on the idea of smoothing, as represented by equation (10), as well as the properties of the spectral window for the smoothing derived earlier, the characteristics of the IESR can be clarified. Because the weights of the spectral window typically concentrate around the oscillator period T_0 as shown in Figures 4 and 7, the value of $(V_{ES}/V_{EB})^2$ at an

Figure 7. Values of the smoothing window $U_e(\bar{\omega}, \omega, 5\%)$ for different bedrock motions and oscillator periods: (a) $T_0 = 0.1$ s; (b) $T_0 = 0.5$ s; and (c) $T_0 = 2$ s. The color version of this figure is available only in the electronic edition.

oscillator period T_0 is typically dominated by the value of $|Tr(\omega)|^2$ at the period T with a value equal to that of the oscillator period T_0 (i.e., $T = T_0$). Therefore, the values of V_{ES}/V_{EB} are generally similar to those of $|Tr(\omega)|$ for the same periods, and their overall shapes are also similar. This conclusion is supported by the results shown in Figures 2 as well as 8 that compares the V_{ES}/V_{EB} values with $|Tr(\omega)|$ considering two simple single-layer soil profiles on bedrock. The values of the site fundamental period T_g , the impedance ratio of the soil layer with respect to the bedrock Im , and the soil damping ratio h are shown in Figure 8. The single-layer soil profiles were chosen to facilitate the understanding, but the derived conclusions can be extended to general soil profiles on bedrock.

In addition, because the spectral window $U_e(\bar{\omega}, \omega, 5\%)$ depends on the bedrock motion, the results of smoothing (i.e., $(V_{ES}/V_{EB})^2$) also change with the bedrock motion. This means that V_{ES}/V_{EB} does not only reflect site effects, but also couples with the effect of bedrock motion, even for linear analysis. This property of V_{ES}/V_{EB} is different from that of the FASR $|Tr(\omega)|$, because in linear analysis, $|Tr(\omega)|$, is completely determined by the site parameters and is independent of the bedrock motion. It is observed from Figure 8 that V_{ES}/V_{EB} strongly depends on the moment magnitude, particularly at long oscillator periods. When the moment magnitude is small, the values of V_{ES}/V_{EB} are largely different from those of $|Tr(\omega)|$, at the same periods. As the moment magnitude M increases, the values of V_{ES}/V_{EB} approach those of $|Tr(\omega)|$, in the overall trend. However, the variation trend of V_{ES}/V_{EB} with M may not be strictly monotonous for all cases. For example, at oscillator periods longer than the site fundamental period as shown in Figure 8b, the values of V_{ES}/V_{EB} temporarily shift away from those of $|Tr(\omega)|$, when M increases from 4 to 6, and finally approach those of $|Tr(\omega)|$,

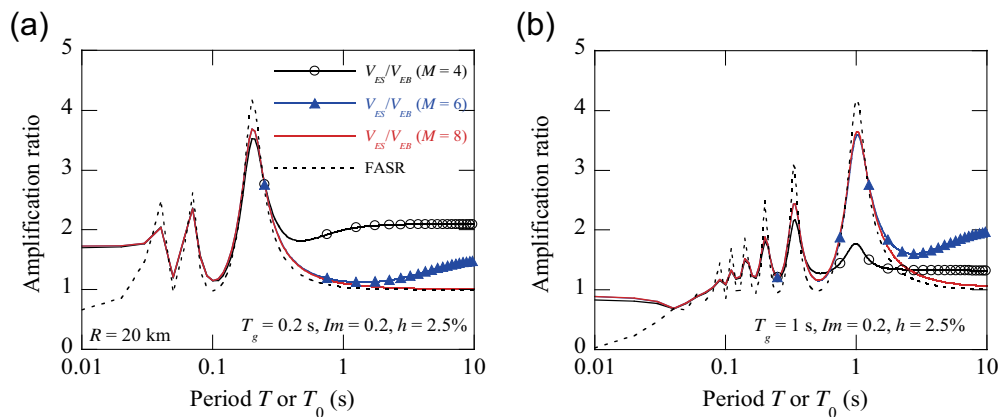


Figure 8. Comparison between the V_{ES}/V_{EB} values and those of the Fourier amplitude spectral ratio (FASR) for different values of the moment magnitude for two sites with the following values of the site fundamental period T_g , impedance ratio l_m , and soil damping ratio h : (a) $T_g = 0.2$ s, $l_m = 0.2$, and $h = 2.5\%$; and (b) $T_g = 1$ s, $l_m = 0.2$, and $h = 2.5\%$. The color version of this figure is available only in the electronic edition.

when M further increases to 8. In addition, it is found from Figure 8 that the relationship between V_{ES}/V_{EB} and $|Tr(\omega)|$ at long oscillator periods also depends on the site parameters. When the site fundamental period is short (Fig. 8a), the values of V_{ES}/V_{EB} at long oscillator periods are greater than those of $|Tr(\omega)|$ for a small moment magnitude. In contrast, when the site fundamental period is long (Fig. 8b), the values of V_{ES}/V_{EB} around the site fundamental period are significantly smaller than those of $|Tr(\omega)|$, for a small moment magnitude.

The dependence of V_{ES}/V_{EB} on the bedrock motion can be explained by the properties of $U_e(\bar{\omega}, \omega, 5\%)$ described earlier. Because the variation of $U_e(\bar{\omega}, \omega, 5\%)$ with the moment magnitude at long oscillator periods is more significant than at short oscillator periods (Fig. 7), V_{ES}/V_{EB} depends more on the moment magnitude at long oscillator periods than at short oscillator periods. In addition, when the moment magnitude is small and the oscillator period is long, the weights of $U_e(\bar{\omega}, \omega, 5\%)$ may scatter around the oscillator period and the predominant period of the FAS as shown in Figure 7c. Therefore, the values of V_{ES}/V_{EB} at long oscillator periods are affected not only by the values of $|Tr(\omega)|$ at the same periods, but they are also largely affected by those at short periods around the predominant period of the FAS. Therefore, when the moment magnitude is small, the values of V_{ES}/V_{EB} at long oscillator periods are significantly different from those of $|Tr(\omega)|$ at the same periods. In addition, because the weights of $U_e(\bar{\omega}, \omega, 5\%)$ shift to the oscillator period T_0 as the moment magnitude M increases (Fig. 7c), the values of V_{ES}/V_{EB} at long oscillator periods approach those of $|Tr(\omega)|$ at the same periods in the overall trend as M increases (Fig. 8). Although the weights of $U_e(\bar{\omega}, \omega, 5\%)$ shift to the oscillator period T_0 as M increases in the overall trend, the variation rule of $U_e(\bar{\omega}, \omega, 5\%)$ with M is not necessarily regular for any specific period. As

shown in Figure 7c, the weights of $U_e(\bar{\omega}, \omega, 5\%)$ around the site fundamental period ($T_g = 1$ s as indicated in Fig. 8b) increase when M increases from 4 to 6 and decrease when M further increases to 8. This results in the largest contribution of the large $|Tr(\omega)|$ values around the site fundamental period to the values of V_{ES}/V_{EB} when $M = 6$ compared with when $M = 4$ and 8. Therefore, at oscillator periods longer than the site fundamental period, as shown in Figure 8b, the values of V_{ES}/V_{EB} temporarily shift away from those of $|Tr(\omega)|$ when M increases to

6 and then approach those of $|Tr(\omega)|$ when M further increases to 8, and the values of V_{ES}/V_{EB} corresponding to $M = 6$ are larger compared with those corresponding to $M = 4$ and 8.

To understand how the relationship between V_{ES}/V_{EB} and $|Tr(\omega)|$ depends on the site parameters shown in Figure 8, the variation of $|Tr(\omega)|$ with the site parameters needs to be understood. When the site fundamental period is short, the values of $|Tr(\omega)|$ at short periods are larger than those at long periods, but the values of $|Tr(\omega)|$ at short periods decrease as the site fundamental period increases (Zhang and Zhao, 2018). In addition, when the moment magnitude is small and the oscillator period is long, the weights of $U_e(\bar{\omega}, \omega, 5\%)$ are also distributed over short periods around the predominant period of the FAS (Fig. 7). Therefore, when the site fundamental period is short, the large $|Tr(\omega)|$ values at short periods significantly contribute to the values of V_{ES}/V_{EB} at long oscillator periods, and values of V_{ES}/V_{EB} at long oscillator periods are generally greater than those of $|Tr(\omega)|$ (Fig. 8a). Similarly, when the site fundamental period is long, small $|Tr(\omega)|$ values at short periods largely affect the values of V_{ES}/V_{EB} around the site fundamental period; thus, the values of V_{ES}/V_{EB} at long oscillator periods are smaller than those of $|Tr(\omega)|$ (Fig. 8b).

Comparison with response spectral ratios

As with the FASR, the ratio of the pseudoacceleration response spectrum on the ground surface to that on the bedrock is also a widely used tool for characterizing site effects. In addition, because the shape of the energy equivalent velocity spectrum is similar to that of the velocity response spectrum, it is of interest in this section, to compare V_{ES}/V_{EB} with the response spectral ratios (RSRs) for pseudoacceleration and velocity. As for the RSR for pseudovelocity, because the pseudovelocity response spectrum is equal to the pseudoacceleration response spectrum multiplied by an oscillator circular frequency $\bar{\omega}$, the

RSR for pseudovelocity should be totally the same as that for pseudoacceleration.

Zhang and Zhao (2021d) provided a theoretical equation of the RSR for pseudoacceleration, RSR_{pa} , based on random vibration theory, and it is expressed as:

$$\frac{S_{paS}(\bar{\omega}, \xi)}{S_{paB}(\bar{\omega}, \xi)} = \sqrt{\int_0^\infty \frac{W_{pa}(\bar{\omega}, \omega, \xi)}{\int_0^\infty W_{pa}(\bar{\omega}, \omega, \xi) d\omega} |Tr(\omega)|^2 d\omega} \times \frac{pf_{pa-os} \sqrt{Db_{pa-rms}}}{pf_{pa-ob} \sqrt{Ds_{pa-rms}}}, \quad (14)$$

in which $S_{paS}(\bar{\omega}, \xi)$ and $S_{paB}(\bar{\omega}, \xi)$ are the pseudoacceleration response spectra at the ground surface and bedrock, respectively; pf_{pa-os} and pf_{pa-ob} are the corresponding peak factors of the oscillator response for the ground-surface and bedrock motions, respectively; and Ds_{pa-rms} and Db_{pa-rms} are the corresponding root mean square durations for the ground-surface and bedrock motions, respectively. The term $W_{pa}(\bar{\omega}, \omega, \xi)$ is the square of the oscillator response FAS, which is expressed as:

$$W_{pa}(\bar{\omega}, \omega, \xi) = |F_B(\omega)|^2 |Hpa(\bar{\omega}, \omega, \xi)|^2. \quad (15)$$

The term $Hpa(\omega, \bar{\omega}, \xi)$ is the oscillator transfer function for the pseudoacceleration, and it is expressed as:

$$|Hpa(\bar{\omega}, \omega, \xi)|^2 = \frac{1}{(2\xi \frac{\omega}{\bar{\omega}})^2 + ((\frac{\omega}{\bar{\omega}})^2 - 1)^2}. \quad (16)$$

Zhang and Zhao (2021d) found that the values of $pf_{pa-os} \sqrt{Db_{pa-rms}} / pf_{pa-ob} \sqrt{Ds_{pa-rms}}$ in equation (14) are typically around unity. Thus, equation (14) is dominated by the former part and can be approximated as:

$$\left(\frac{S_{paS}(\bar{\omega}, \xi)}{S_{paB}(\bar{\omega}, \xi)} \right)^2 \approx \int_0^\infty U_{pa}(\bar{\omega}, \omega, \xi) |Tr(\omega)|^2 d\omega, \quad (17)$$

$$U_{pa}(\bar{\omega}, \omega, \xi) = \int_0^\infty \frac{W_{pa}(\bar{\omega}, \omega, \xi)}{\int_0^\infty W_{pa}(\bar{\omega}, \omega, \xi) d\omega} d\omega. \quad (18)$$

Similarly, a theoretical equation of the RSR for velocity, RSR_v , can be obtained according to the velocity response spectrum derived based on random vibration theory (Zhang and Zhao, 2021b), which is expressed as:

$$\left(\frac{S_{vS}(\bar{\omega}, \xi)}{S_{vB}(\bar{\omega}, \xi)} \right)^2 = \int_0^\infty U_v(\bar{\omega}, \omega, \xi) |Tr(\omega)|^2 d\omega \times \left(\frac{pf_{v-os} \sqrt{Db_{v-rms}}}{pf_{v-ob} \sqrt{Ds_{v-rms}}} \right)^2, \quad (19)$$

$$U_v(\bar{\omega}, \omega, \xi) = \int_0^\infty \frac{W_v(\bar{\omega}, \omega, \xi)}{\int_0^\infty W_v(\bar{\omega}, \omega, \xi) d\omega} d\omega, \quad (20)$$

in which $S_{vS}(\bar{\omega}, \xi)$ and $S_{vB}(\bar{\omega}, \xi)$ are the velocity response spectra at the ground surface and bedrock, respectively; pf_{v-os} and pf_{v-ob} are the corresponding peak factors of the oscillator response for the ground-surface and bedrock motions, respectively; and Ds_{v-rms} and Db_{v-rms} are the corresponding root-mean-square durations for the ground-surface and bedrock motions, respectively. The term $W_v(\bar{\omega}, \omega, \xi)$ is expressed as:

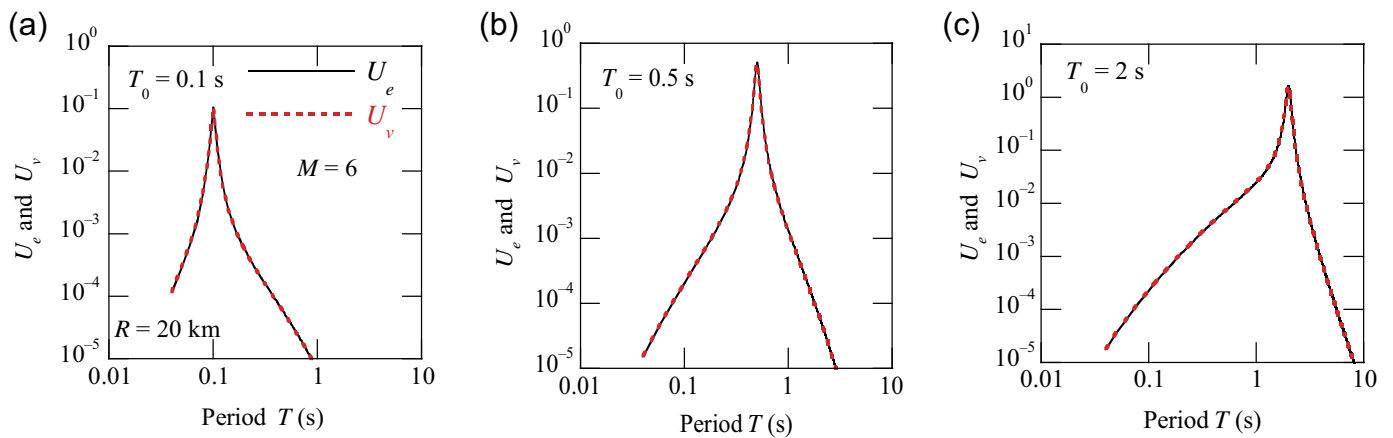
$$W_v(\bar{\omega}, \omega, \xi) = |F_B(\omega)|^2 |Hv(\bar{\omega}, \omega, \xi)|^2, \quad (21)$$

and the term $|Hv(\bar{\omega}, \omega, \xi)|^2$ is expressed as:

$$|Hv(\bar{\omega}, \omega, \xi)|^2 = \frac{\omega^2}{(2\xi \bar{\omega})^2 + (\omega^2 - \bar{\omega}^2)^2}. \quad (22)$$

By comparing equations (13), (17), and (19), their forms can be found to be extremely similar, if the term $pf_{v-os} \sqrt{Db_{v-rms}} / pf_{v-ob} \sqrt{Ds_{v-rms}}$ in equation (19) is also ignored. Equations (17) and (19) also represent procedures for smoothing a function, $|Tr(\omega)|^2$ is also the function to be smoothed, and $U_{pa}(\bar{\omega}, \omega, \xi)$ and $U_v(\bar{\omega}, \omega, \xi)$ are the spectral windows for smoothing that satisfy the conditions $\int_0^\infty U_{pa}(\bar{\omega}, \omega, \xi) d\omega = 1$ and $\int_0^\infty U_v(\bar{\omega}, \omega, \xi) d\omega = 1$. In addition, it can be known that the spectral window for RSR_v , $U_v(\bar{\omega}, \omega, \xi)$ (equations 20 and 21), is the same as that for V_{ES}/V_{EB} , $U_e(\bar{\omega}, \omega, \xi)$ (equations 11 and 12). This is because $|Hv(\bar{\omega}, \omega, \xi)|^2$ (equation 22) is proportional to $-Re[Hv(\bar{\omega}, \omega, \xi)]$ (equation 5) for a specific oscillator period, that is, $-Re[Hv(\bar{\omega}, \omega, \xi)] = 2\xi \bar{\omega} |Hv(\bar{\omega}, \omega, \xi)|^2$. The representative results of $U_e(\bar{\omega}, \omega, \xi)$ and $U_v(\bar{\omega}, \omega, \xi)$ considering three oscillator periods are shown in Figure 9. This implies that the RSR_v will be the same as V_{ES}/V_{EB} if $pf_{v-os} \sqrt{Db_{v-rms}} / pf_{v-ob} \sqrt{Ds_{v-rms}}$ in equation (19) is also assumed to be unity. However, because this assumption has never been systematically studied by previous studies, more realistic comparisons of the RSR_v with V_{ES}/V_{EB} based on real seismic records are conducted in the section **Properties of IESR Based on Real Seismic Records**.

However, the spectral window for the RSR_{pa} ($U_{pa}(\bar{\omega}, \omega, \xi)$) is different from that for V_{ES}/V_{EB} ($U_e(\bar{\omega}, \omega, \xi)$). The spectral window for the RSR_{pa} is determined by the bedrock-motion FAS $F_B(\omega)$ and the oscillator transfer function for pseudoacceleration $|Hpa(\bar{\omega}, \omega, \xi)|$ (equations 15 and 18), whereas the spectral window for V_{ES}/V_{EB} is determined by $F_B(\omega)$ and the real part of the oscillator transfer function for the relative velocity $-Re[Hv(\bar{\omega}, \omega, \xi)]$ (equations 11 and 12). Therefore, the main difference between the RSR_{pa} and V_{ES}/V_{EB} can be deduced as the difference in oscillator transfer functions. Figure 10 shows a comparison between $-Re[Hv(\bar{\omega}, \omega, \xi)]$ and $|Hpa(\bar{\omega}, \omega, \xi)|^2$, for which the oscillator period T_0 was set to 1 s, and the oscillator damping ratio ξ was set to 5%. It is found that similar to $-Re[Hv(\bar{\omega}, \omega, 5\%)]$, $|Hpa(\bar{\omega}, \omega, 5\%)|^2$ also has a peak at the oscillator period T_0 . However, in contrast to $-Re[Hv(\bar{\omega}, \omega, 5\%)]$, $|Hpa(\bar{\omega}, \omega, 5\%)|^2$ decreases faster than $-Re[Hv(\bar{\omega}, \omega, 5\%)]$ toward



zero as the period T decreases, and $|Hpa(\bar{\omega}, \omega, 5\%)|^2$ decreases toward unity instead of zero as the period T increases.

According to the properties of the two oscillator transfer functions, the relationships between the two spectral windows for smoothing (i.e., $U_{pa}(\bar{\omega}, \omega, 5\%)$ and $U_e(\bar{\omega}, \omega, 5\%)$), can be understood. Figure 11 presents the representative results of $U_{pa}(\bar{\omega}, \omega, 5\%)$ and $U_e(\bar{\omega}, \omega, 5\%)$ considering various oscillator periods and moment magnitudes. Because, similar to $-Re[Hv(\bar{\omega}, \omega, 5\%)]$, $|Hpa(\bar{\omega}, \omega, 5\%)|^2$ has a peak at the oscillator period T_0 , a peak also occurs in $U_{pa}(\bar{\omega}, \omega, 5\%)$ around the oscillator period T_0 . This means that the weights of $U_{pa}(\bar{\omega}, \omega, 5\%)$ are also concentrated around the oscillator period T_0 . However, because $|Hpa(\bar{\omega}, \omega, 5\%)|^2$ decreases faster than $-Re[Hv(\bar{\omega}, \omega, 5\%)]$ toward zero as the period T decreases, the values (or weights) of $U_{pa}(\bar{\omega}, \omega, 5\%)$ decrease faster than those of $U_e(\bar{\omega}, \omega, 5\%)$ at periods shorter than the oscillator period T_0 . The fast decay of $|Hpa(\bar{\omega}, \omega, 5\%)|^2$ at short periods prevents $U_{pa}(\bar{\omega}, \omega, 5\%)$ from having a peak around the predominant period of the FAS (as $U_e(\bar{\omega}, \omega, 5\%)$ does), for a small magnitude and long oscillator period (Fig. 11d). In addition, because $|Hpa(\bar{\omega}, \omega, 5\%)|^2$ decreases toward unity (instead of zero as $-Re[Hv(\bar{\omega}, \omega, 5\%)]$ does) with increasing period T , the values (or weights) of $U_{pa}(\bar{\omega}, \omega, 5\%)$ are larger than those of $U_e(\bar{\omega}, \omega, 5\%)$ at periods longer than the oscillator period T_0 .

In addition, as with $U_e(\bar{\omega}, \omega, 5\%)$, $U_{pa}(\bar{\omega}, \omega, 5\%)$ also varies with bedrock motion. Because long-period components of the FAS increase relative to the short-period components as the moment magnitude increases, the long-period components of $U_{pa}(\bar{\omega}, \omega, 5\%)$ also increase with increasing moment magnitude. However, their degrees of variation with bedrock motion are different because of the different oscillator transfer functions. At short oscillator periods (Fig. 11a–c), because $|Hpa(\bar{\omega}, \omega, 5\%)|^2$ decreases toward unity (instead of zero) with increasing period T , the long-period components of $U_{pa}(\bar{\omega}, \omega, 5\%)$ increase more obviously than those of $U_e(\bar{\omega}, \omega, \xi)$ with increasing moment magnitude. At long oscillator periods (Fig. 11d–f), because $-Re[Hv(\bar{\omega}, \omega, 5\%)]$ decreases more slowly than $|Hpa(\bar{\omega}, \omega, 5\%)|^2$ toward zero with decreasing period T , the short-period components of $U_e(\bar{\omega}, \omega, \xi)$ decrease more

Figure 9. Comparison of the smoothing windows $U_e(\bar{\omega}, \omega, 5\%)$ and $U_v(\bar{\omega}, \omega, 5\%)$ for cases with the oscillator period T_0 : (a) $T_0 = 0.1$ s; (b) $T_0 = 0.5$ s; and (c) $T_0 = 2$ s. The color version of this figure is available only in the electronic edition.

obviously than those of $U_{pa}(\bar{\omega}, \omega, 5\%)$ with increasing moment magnitude. In addition, the difference between the variations in $U_{pa}(\bar{\omega}, \omega, 5\%)$ and $U_e(\bar{\omega}, \omega, 5\%)$ with bedrock motion is more obvious at long oscillator periods than at short oscillator periods, which can be clearly observed in general vertical coordinates as shown in Figure 12.

Based on the properties of $U_{pa}(\bar{\omega}, \omega, 5\%)$ and $U_e(\bar{\omega}, \omega, 5\%)$, the relationship between V_{ES}/V_{EB} and RSR_{pa} can be clarified. Because, similar to $U_e(\bar{\omega}, \omega, 5\%)$, the weights of $U_{pa}(\bar{\omega}, \omega, 5\%)$ also concentrate around the oscillator period T_0 , the value of the RSR_{pa} at an oscillator period T_0 is also dominated by the value of $|Tr(\omega)|$ at the period T with a value equal to that of the oscillator period T_0 (i.e., $T = T_0$). Therefore, the values of the RSR_{pa} are also generally similar to those of $|Tr(\omega)|$ at the same periods, and their overall shapes are similar. This means that the values and overall shapes of $|Tr(\omega)|$, the RSR_{pa} , and V_{ES}/V_{EB} are generally similar. This conclusion is supported by Figure 13, which shows the values of the RSR_{pa} , $|Tr(\omega)|$, and V_{ES}/V_{EB} for the two soil profiles used in Figure 8. Here, V_{ES}/V_{EB} and RSR_{pa} are both calculated directly using the FAS (Boore, 2003) as input based on equations (13) and (17), respectively. In addition, because similar to $U_e(\bar{\omega}, \omega, 5\%)$, $U_{pa}(\bar{\omega}, \omega, 5\%)$ varies with bedrock motion, the RSR_{pa} is also dependent on the bedrock motion. However, because the degrees to which the two smoothing windows vary with bedrock motion are different, the degrees of variation of V_{ES}/V_{EB} and RSR_{pa} are also different. At short oscillator periods, because the variation in $U_{pa}(\bar{\omega}, \omega, 5\%)$ with respect to the moment magnitude is more significant than the corresponding variation in $U_e(\bar{\omega}, \omega, 5\%)$, the RSR_{pa} varies more significantly than V_{ES}/V_{EB} with the moment magnitude. At long oscillator periods, because the variation in $U_e(\bar{\omega}, \omega, 5\%)$ with the moment magnitude is more significant than the corresponding variation

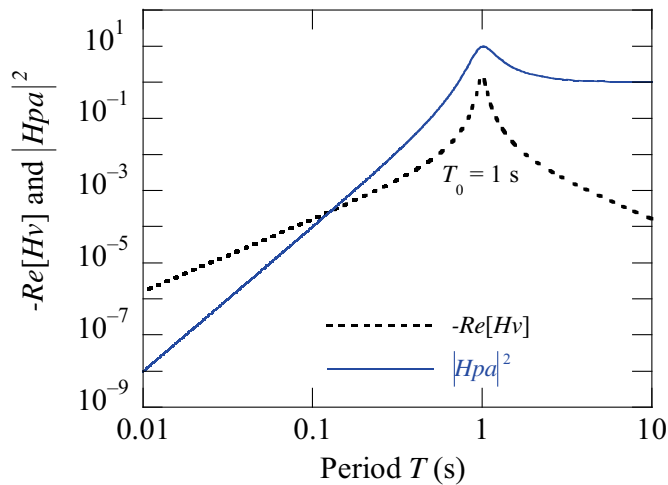


Figure 10. Comparison between the oscillator transfer function for the pseudoacceleration and the real part of the oscillator transfer function for the relative velocity. The color version of this figure is available only in the electronic edition.

in $U_{pa}(\tilde{\omega}, \omega, 5\%)$, V_{ES}/V_{EB} varies with the moment magnitude more significantly than RSR_{pa} .

PROPERTIES OF IESR BASED ON REAL SEISMIC RECORDS

The properties of IESR derived earlier are further confirmed based on actual seismic records from adjacent soil and rock sites. Zhang and Zhao (2021a) carefully selected 10 pairs of adjacent soil and rock sites from the K-NET and KiK-net of Japan. The soil and rock sites have surface-layer shear-wave velocities below and greater than 400 m/s, respectively, according to the definition of the Japanese Seismic Design Code (2000). In addition, the soil sites were selected to be as close as possible to the rock site. Among the selected 10 pairs of soil and rock sites, the farthest distance from the rock to soil sites is 4.16 km, and the shortest distance is 0.01 km. The characteristics of the 10 pairs of selected soil and rock sites are detailed in Table 1.

Zhang and Zhao (2021a) selected ground-motion records on the 10 pairs from 1996 to 2016 based on the criteria that the peak acceleration is above 5 gal, and the epicentral distance is farther than 10 times the distance between the rock and adjacent soil sites and less than 300 km. In this study, ground motions records on the 10 pairs are updated till May 2021 based on the same criteria. Finally, 642 ground-motion records from 297 earthquakes are used in this study. There are two components for each ground-motion record: north–south and east–west. Therefore, this study used 1284 earthquake time histories. The distributions of magnitudes, M_{JMA} , and epicentral distances R_e of the used earthquakes are shown in Figure 14. The earthquakes have a wide range of magnitudes and epicentral distances.

Then, input energy spectra, response spectra, and Fourier amplitude spectra of all selected ground-motion records are calculated. A 5% oscillator damping ratio is used for the calculation of the input energy spectra and response spectra. A Parzen window function with a bandwidth of 0.3 Hz is used to smooth the Fourier amplitudes. Then, the geometric means of the two components in east–west and north–south directions for each seismic record are computed. Finally, the IESR, RSR_{pa} , RSR_v , and FASR are calculated as the quotients of the spectra for the soil sites compared with those for the rock sites. Zhang and Zhao (2021a) observed that the spectral ratios for five pairs of sites have obvious peaks, whereas those for the other five pairs show no obvious peaks. For the five pairs with no obvious peaks, the results of IESR, RSR_{pa} , RSR_v , and FASR are all around unity and nearly the same, which are not shown in this article. The comparisons of the average values of V_{ES}/V_{EB} , RSR_{pa} , RSR_v , and FASR for the five neighboring soil–rock pairs with obvious peaks are shown in Figure 15. It is observed that the overall shapes and values of the average V_{ES}/V_{EB} , RSR_{pa} , RSR_v , and FASR at the same periods are similar. The overall shapes of V_{ES}/V_{EB} , RSR_{pa} , and RSR_v are smoother than that of the FASR. These phenomena are consistent with those obtained based on theoretical analyses.

To confirm the dependence of the V_{ES}/V_{EB} on the bedrock motion, the selected ground motions introduced earlier are classified into three groups according to magnitude and epicentral distance, as shown in Figure 16 and listed in table 2 of Zhang and Zhao (2021a). In group 1, seismic motions have small magnitudes and short distances; in group 2, seismic motions have large magnitudes and short distances; and in group 3, seismic motions have large magnitudes and long distances. Therefore, by comparing the results from groups 1 to 3, the effects of magnitude and epicentral distance can be investigated.

The V_{ES}/V_{EB} , RSR_{pa} , RSR_v , and FASR in the same group for each pair of soil and rock sites are averaged, and the average values of V_{ES}/V_{EB} , RSR_{pa} , RSR_v , and FASR for each group are compared in Figure 16. Figure 16 also shows the comparisons for the five pairs of soil and rock sites in which the V_{ES}/V_{EB} , RSR_{pa} , RSR_v , and FASR have obvious peaks. The results of some groups for some sites are lacking, as shown in Figure 16. This is because, among the selected seismic motion data described previously, there are no data belonging to these groups for these sites, although as many seismic records as possible are selected. It can be confirmed that values of V_{ES}/V_{EB} are significantly different from those of FASR for small magnitude (group 1) at long oscillator periods, and values of V_{ES}/V_{EB} approach those of FASR with increasing magnitude (group 2). In addition, the values of V_{ES}/V_{EB} are generally larger than those of FASR for small magnitude (group 1). This is because the site fundamental periods of the 10 soil sites are relatively short ($T_g < 0.39$ s). For long site fundamental

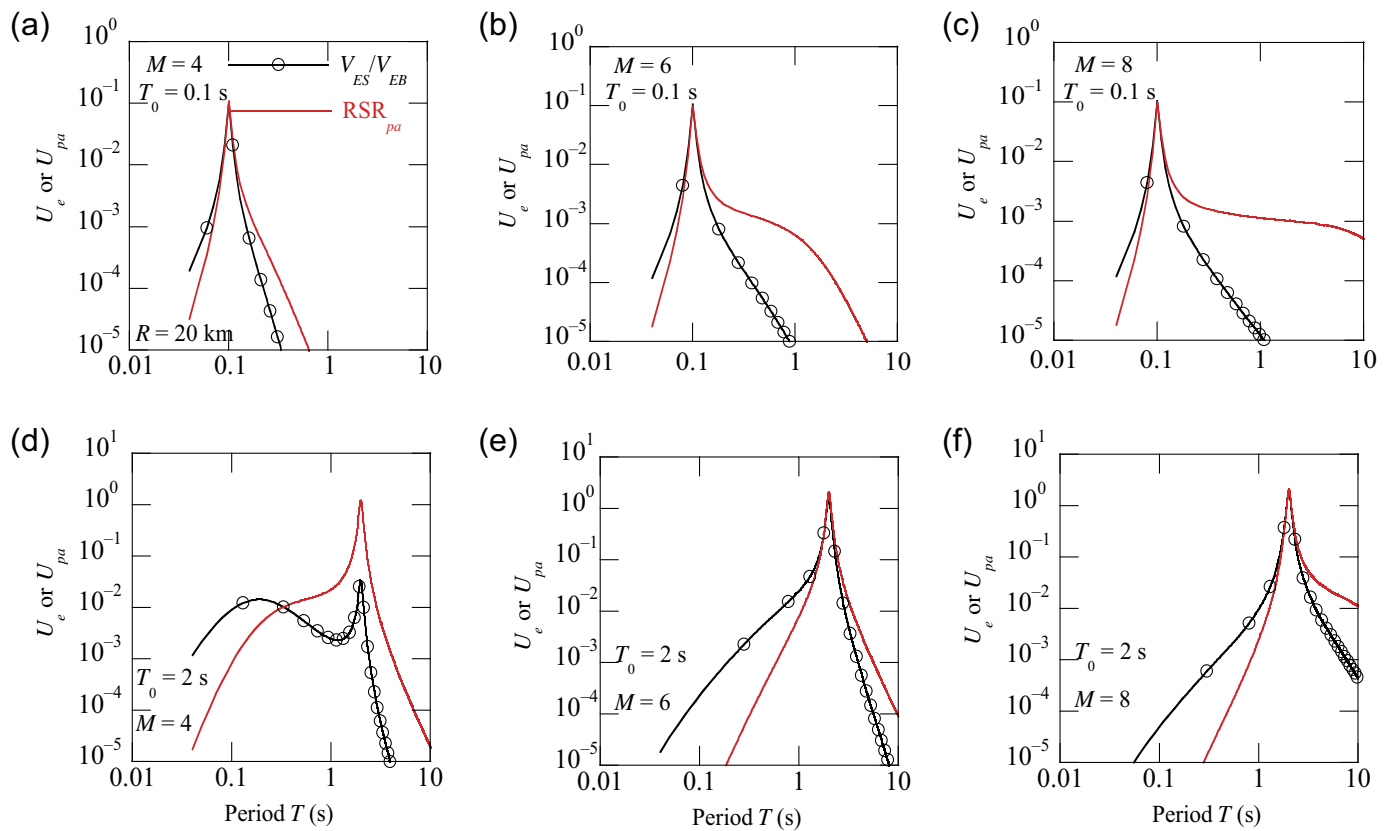
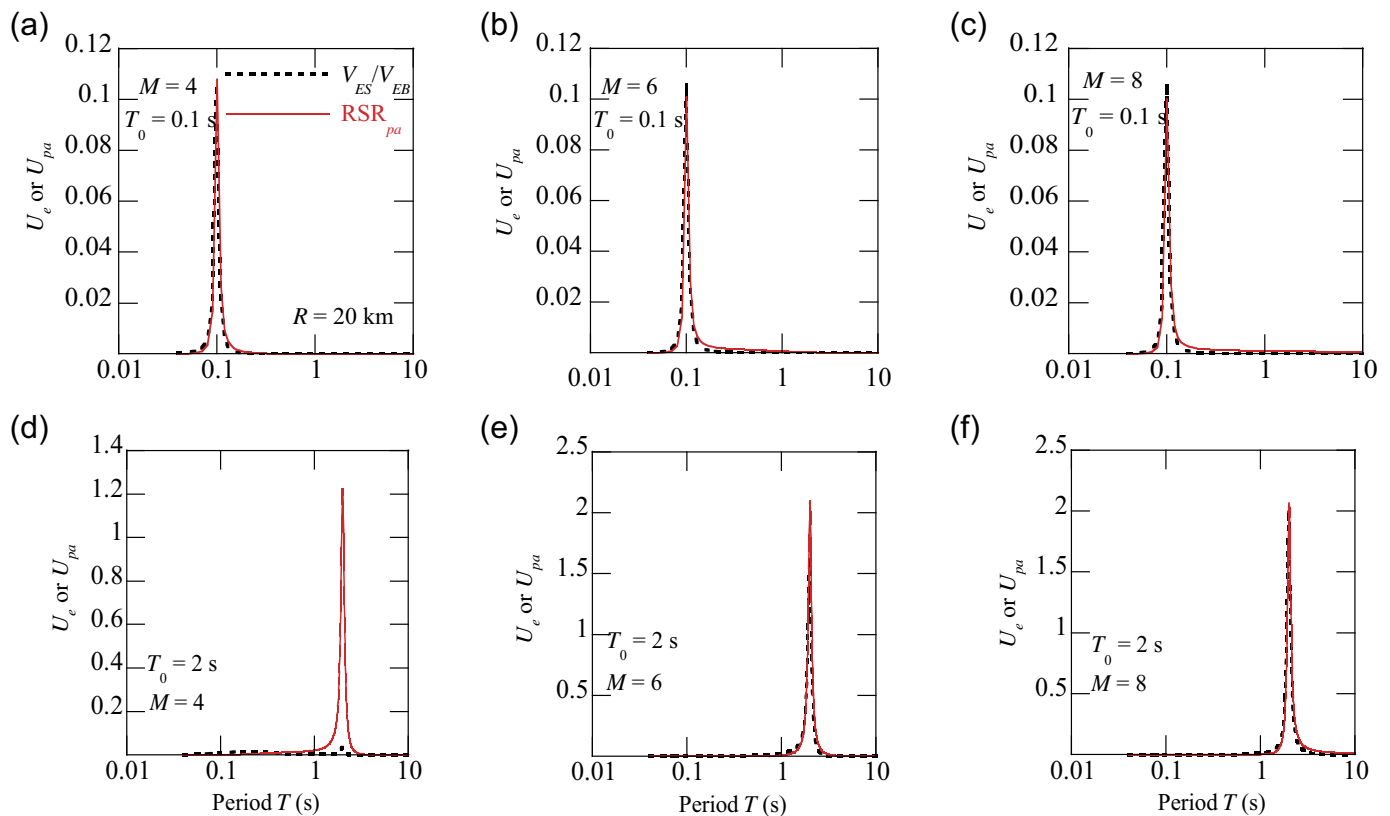


Figure 11. Logarithmic comparison between the smoothing windows for response spectral ratio for pseudoacceleration (RSR_{pa}) and V_{ES}/V_{EB} for (a) $T_0 = 0.1$ s, $M = 4$; (b) $T_0 = 0.1$ s, $M = 6$; (c) $T_0 = 0.1$ s, $M = 8$; (d) $T_0 = 2$ s, $M = 4$; (e) $T_0 = 2$ s, $M = 6$; and (f) $T_0 = 2$ s, $M = 8$. The color version of this figure is available only in the electronic edition.

TABLE 1
Characteristics of the Selected 10 Pairs of Neighboring Soil and Rock Sites

Station ID		Coordinates			Site Conditions	
Name	Code	Longitude	Latitude	Distance (km)	S (m/s)	V_{S30} (m/s)
1	AOMH03	140.9896	41.234	4.10	530	653.7
	AOM006	140.9972	41.1976		100	264.8
2	CHBH20	140.0997	35.0882	3.04	1800	1909.1
	CHB020	140.1022	35.1155		150	134.4
3	ISKH04	136.7176	37.1902	4.16	440	443.5
	ISK006	136.6897	37.1602		260	344.0
4	YMGH01	131.5618	34.0494	3.22	1000	1387.7
	YMG013	131.5348	34.031		70	185.4
5	NGSH06	129.8625	32.6999	4.15	900	1421.1
	NGS010	129.8763	32.7353		150	371.6
6	GIFH20	137.2531	35.7991	0.84	460	809.9
	GIF010	137.245	35.8029		150	440.9
7	GIFH14	137.5174	36.2493	0.01	440	627.4
	GIF004	137.5174	36.2492		230	452.7
8	ISKH07	136.6357	36.515	3.07	440	440.0
	ISK010	136.6431	36.5419		110	388.2
9	SRCH10	142.0085	42.993	0.03	480	1026.8
	HKD123	142.0085	42.9933		110	627.1
10	MIE014	136.1687	34.0638	0.02	880	1009.4
	MIEH05	136.1689	34.0637		170	590.1



periods, the opposite conclusion may be drawn according to the theoretical analyses earlier. However, due to the absence of long-fundamental-period sites, the conclusion cannot be confirmed in this study. Moreover, it can be confirmed that V_{ES}/V_{EB} varies more significantly than RSR_{pa} at long oscillator periods with the magnitude. In addition, the variation of V_{ES}/V_{EB} with the epicentral distance is found to be not that obvious by comparing the results in groups 2 and 3. In addition, although the values of V_{ES}/V_{EB} are not the same as those of RSR_v , they are relatively more similar compared to other spectral ratios. The similarity between V_{ES}/V_{EB} and RSR_v varies with the oscillator period, magnitude, distance, and site. In general, all the conclusions obtained based on theoretical analyses can be confirmed based on actual seismic ground motions recorded on the adjacent soil and rock sites.

CONCLUSIONS

This study presented a theoretical relationship between the site amplification ratio of the input energy spectrum for an SDOF and that of the FAS, which generated a better theoretical understanding of site effects on the input energy spectrum. The derived theoretical relationship between the IESR and the FASR was verified based on real seismic records and site response analyses. The characteristics of the IESR were comprehensively explored and explained based on the derived relationship and confirmed using real seismic records, and they were compared to those of the FASR and the RSR for

Figure 12. Linear comparison between the smoothing windows for RSR_{pa} and V_{ES}/V_{EB} for (a) $T_0 = 0.1$ s, $M = 4$; (b) $T_0 = 0.1$ s, $M = 6$; (c) $T_0 = 0.1$ s, $M = 8$; (d) $T_0 = 2$ s, $M = 4$; (e) $T_0 = 2$ s, $M = 4$; and (f) $T_0 = 2$ s, $M = 8$. The color version of this figure is available only in the electronic edition.

pseudoacceleration and velocity. The main conclusions of this study are summarized as follows:

1. The IESR is the smoothed squared form of the FASR, and the spectral window for smoothing is determined by the FAS of the bedrock motion and the oscillator transfer function for the relative velocity.
2. The overall shape of the square root of the IESR (i.e., V_{ES}/V_{EB}) is considerably similar to that of the FASR as well as the RSR for pseudoacceleration and velocity.
3. The IESR depends largely on the bedrock motion, particularly at long oscillator periods. The V_{ES}/V_{EB} values are significantly different from those of the FASR for small moment magnitudes, and they approach those of the FASR in the overall trend as the moment magnitude increases. For small moment magnitudes, the V_{ES}/V_{EB} values at long oscillator periods may be larger or smaller than those of the FASR depending on the considered site. This conclusion implies that when a V_{ES}/V_{EB} model is developed to reflect site effects on the input energy spectrum in seismic design or the attenuation model, not only site conditions, but also properties of the input bedrock motion should be considered. Maybe, a

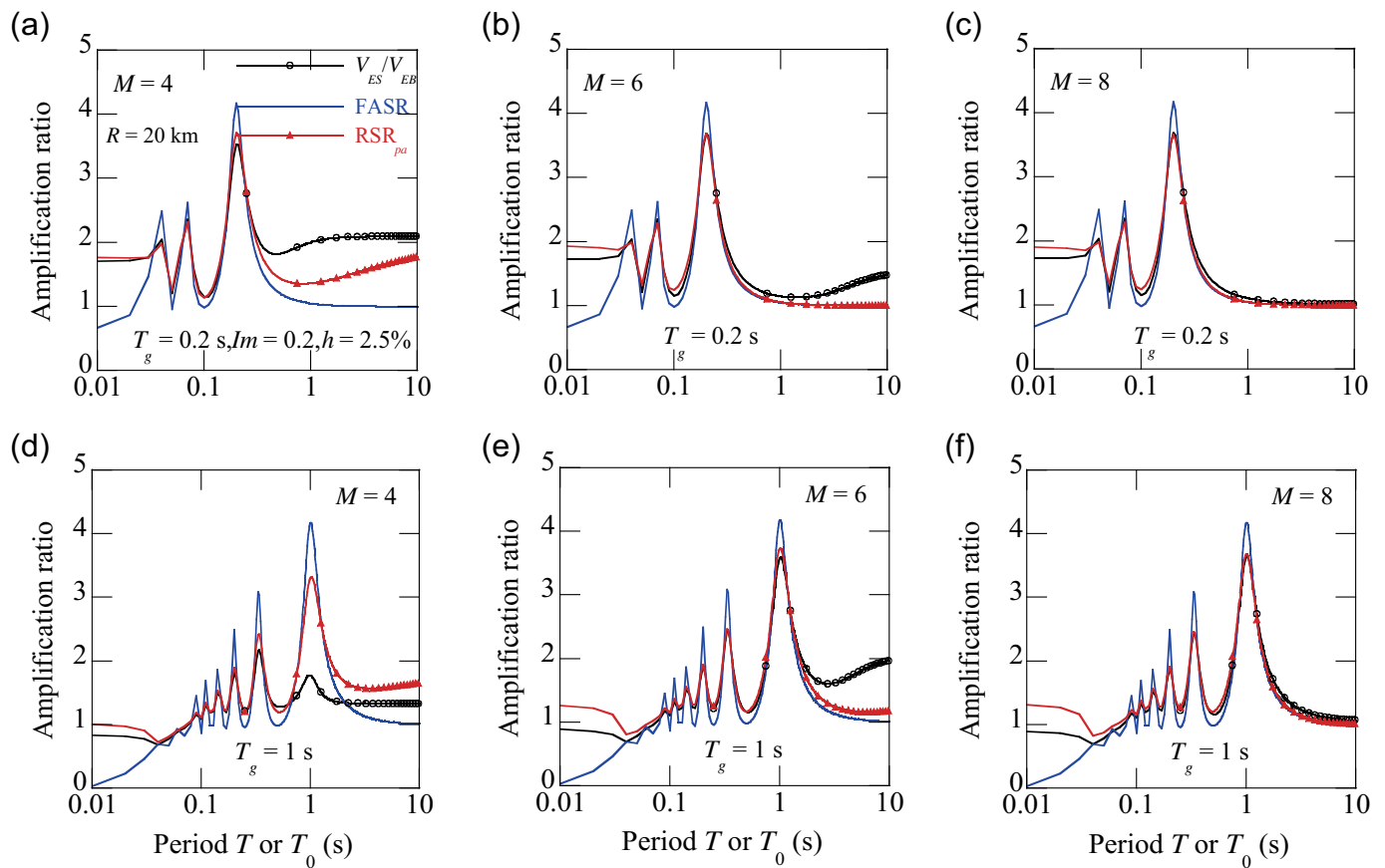


Figure 13. Comparison between the values of V_{ES}/V_{EB} , RSR_{pa} , and the FASR considering different values of the moment magnitude for (a) $M = 4$, $T_g = 0.2$ s; (b) $M = 6$, $T_g = 0.2$ s; (c) $M = 8$, $T_g = 0.2$ s; (d) $M = 4$, $T_g = 1$ s; (e) $M = 6$, $T_g = 1$ s; and (f) $M = 8$, $T_g = 1$ s. The color version of this figure is available only in the electronic edition.

V_{ES}/V_{EB} model for seismic design should be developed for a specific magnitude range considered for design, and the V_{ES}/V_{EB} term in the attenuation model should include magnitude as a parameter.

- The dependency of the IESR on bedrock motion is obviously more significant than that of the RSR for pseudoacceleration at long oscillator periods.

DATA AND RESOURCES

All strong-motion records used in this study can be downloaded from <http://www.kyoshin.bosai.go.jp/> (last accessed November 2021). The information for unpublished report is “Kozo System, Inc. SNAP-WAVE, Software to generate input seismic waves for seismic response analysis of structures, Japan.”

DECLARATION OF COMPETING INTERESTS

The authors acknowledge that there are no conflicts of interest recorded.

ACKNOWLEDGMENTS

This study was partially supported by the National Natural Science Foundation of China (Grant Numbers 51738001 and 52278135). This study used strong-motion records from Kyoshin net (K-NET) and Kiban–Kyoshin network (KiK-net). The authors are grateful for the financial support and earthquake data. The authors also thank Associate Editor Hiroshi Kawase and two anonymous reviewers for their perceptive and useful comments, which led to significant improvements in the article.

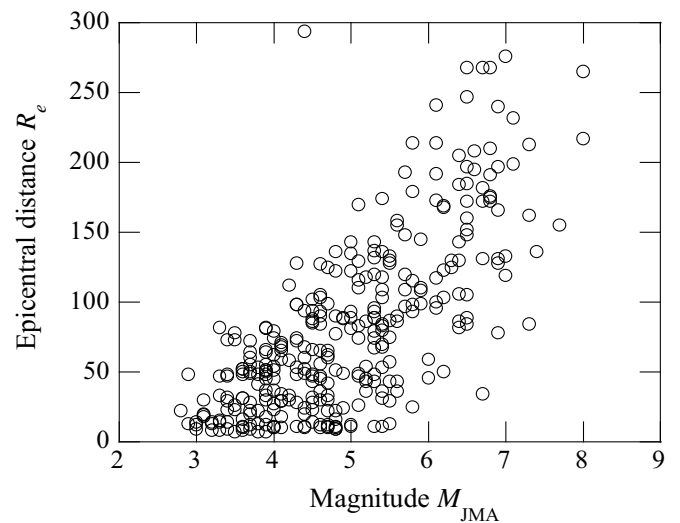


Figure 14. Distributions of magnitude and epicentral distance of the selected earthquakes.

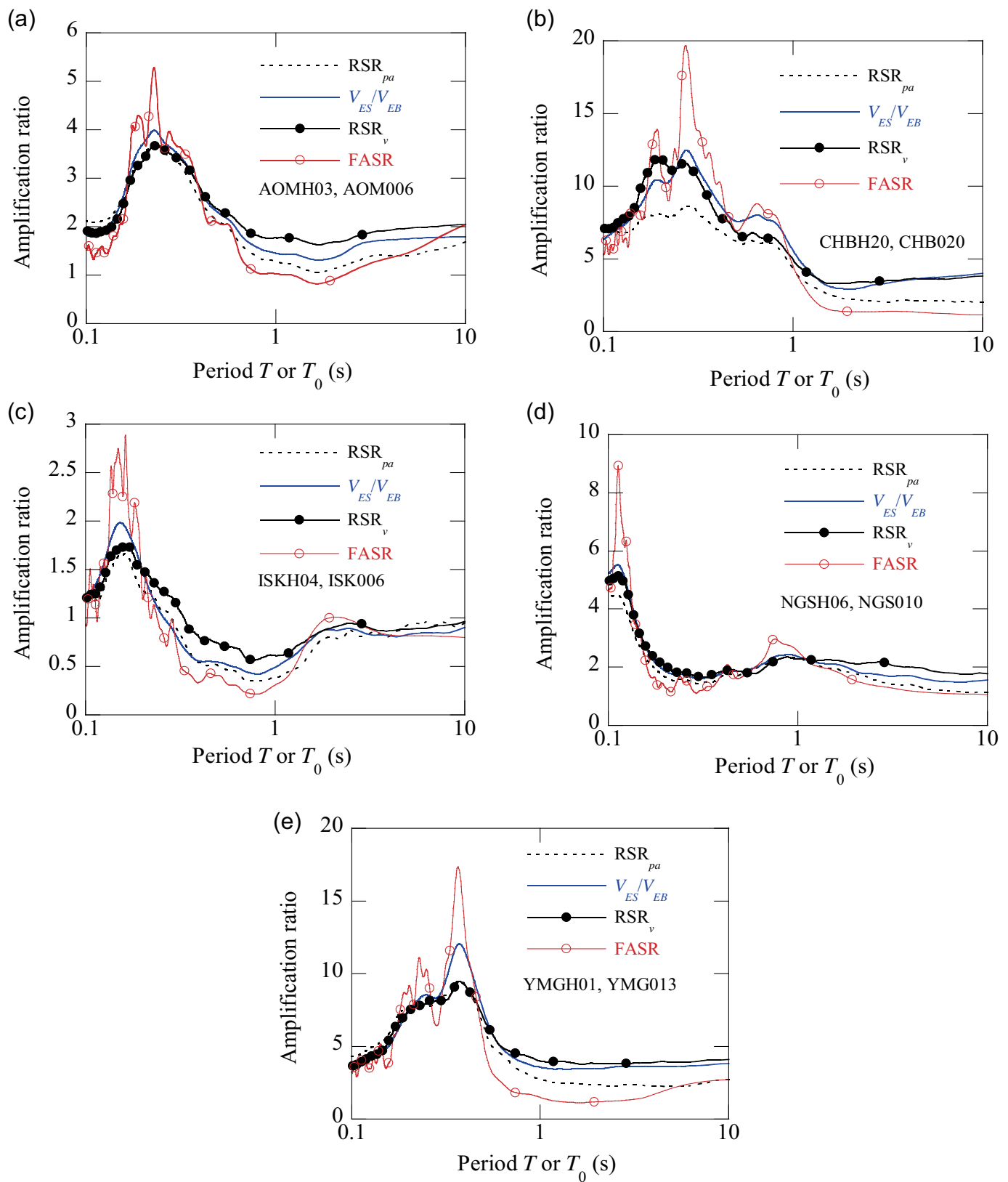


Figure 15. Comparison of results of V_{ES}/V_{EB} with those of RSR_{pa} , RSR_v , and FASR based on real seismic records: (a) AOMH03 and AOM006; (b) CHBH20 and CHB020; (c) ISKH04 and ISK006; (d) NGSH06, NGS010;

(e) YMGH01 and YMG013. The color version of this figure is available only in the electronic edition.

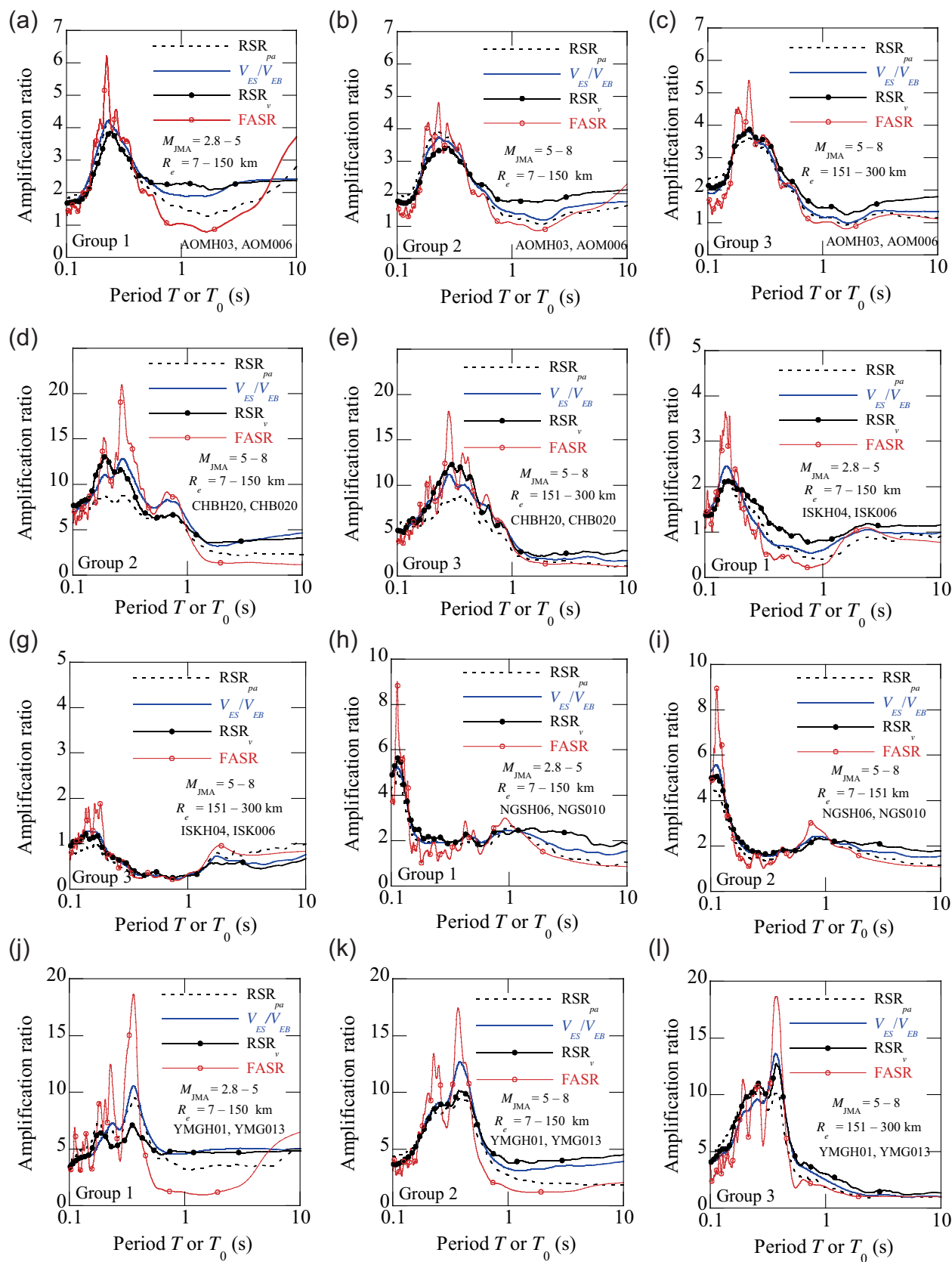


Figure 16. Effects of magnitude and epicentral distance on the relationship of V_{ES}/V_{EB} with RSR_{pa} , RSR_v , and FASR based on real seismic records:

(a) Group 1, AOMH03 and AOM006; (b) Group 2, AOMH03 and AOM006; (c) Group 3, AOMH03 and AOM006; (d) Group 2, CHBH20 and CHB020; (e) Group 3, CHBH20 and CHB020; (f) Group 1, ISKH04 and ISK006;

(g) Group 3, ISKH04 and ISK006; (h) Group 1, NGSH06 and NGS010; (i) Group 2, NGSH06 and NGS010; (j) Group 1, YMGH01 and YMG013; (k) Group 2, YMGH01 and YMG013; (l) Group 3, YMGH01 and YMG013.

The color version of this figure is available only in the electronic edition.

REFERENCES

- Acun, B., and H. Sucuoğlu (2010). Performance of reinforced concrete columns designed for flexure under severe displacement cycles, *ACI Struct. J.* **107**, no. 3, 364–371.
- Akiyama, H. (1985). *Earthquake-Resistant Limit-State Design for Buildings*, University of Tokyo Press, Tokyo, Japan.
- Akiyama, H., Z. Y. Yang, and H. Kitamura (1993). A proposal of design energy spectra allowing for rock and soil conditions, *J. Struct. Constr. Eng. AIJ* **450**, 59–69.
- Alici, F. S., and H. Sucuoğlu (2016). Prediction of input energy spectrum: Attenuation models and velocity spectrum scaling, *Earthq. Eng. Struct. Dynam.* **45**, 2137–2161.
- Alici, F. S., and H. Sucuoğlu (2018). Elastic and inelastic near-fault input energy spectra, *Earthq. Spectra* **34**, no. 2, 611–637.
- Amiri, G. G., G. A. Darzi, and J. V. Amiri (2008). Design elastic input energy spectra based on Iranian earthquakes, *Can. J. Civ. Eng.* **35**, 635–646.
- Aoi, S., T. Kunugi, H. Nakamura, and H. Fujiwara (2011). Deployment of new strong motion seismographs of K-NET and KiK-net, in *Geotechnical, Geological and Earthquake Engineering*, A. Atilla, J. J. Bommer, J. Bray, K. Pitilakis, and S. Yasuda (Editors), Vol. 12, Springer, 167–186.
- Benavent-Climent, A. (2007). An energy-based damage model for seismic response of steel structures, *Earthq. Eng. Struct. Dynam.* **36**, 1049–1064.
- Benavent-Climent, A., F. López-Almansa, and D. A. Bravo-González (2010). Design energy input spectra for moderate-to-high seismicity regions based on Colombian earthquakes, *Soil Dynam. Earthq. Eng.* **30**, 1129–1148.
- Benavent-Climent, A., L. G. Pujades, and F. López-Almansa (2002). Design energy input spectra for moderate-seismicity regions, *Earthq. Eng. Struct. Dynam.* **31**, 1151–1172.
- Boore, D. M. (2003). Simulation of ground motion using the stochastic method, *Pure Appl. Geophys.* **160**, 635–676.
- Boore, D. M., and E. M. Thompson (2015). Revisions to some parameters used in stochastic-method simulations of ground motion, *Bull. Seismol. Soc. Am.* **105**, 1029–1041.
- Chai, Y. H., and P. Fajfar (2000). A procedure for estimating input energy spectra for seismic design, *J. Earthq. Eng.* **4**, no. 4, 539–561.
- Chapman, M. C. (1999). On the use of elastic input energy for seismic hazard analysis, *Earthq. Spectra* **15**, no. 4, 607–635.
- Cheng, Y., A. Lucchini, and F. Mollaioli (2014). Proposal of new ground-motion prediction equations for elastic input energy spectra, *Earthq. Struct.* **7**, no. 4, 485–510.
- Cheng, Y., A. Lucchini, and F. Mollaioli (2020). Ground-motion prediction equations for constant-strength and constant-ductility input energy spectra, *Bull. Earthq. Eng.* **18**, 37–55.
- Chou, C. C., and C. M. Uang (2000). Establishing absorbed energy spectra—an attenuation approach, *Earthq. Eng. Struct. Dynam.* **29**, 1441–1455.
- Decanini, L. D., and F. Mollaioli (1998). Formulation of elastic earthquake input energy spectra, *Earthq. Eng. Struct. Dynam.* **27**, 1503–1522.
- Decanini, L. D., and F. Mollaioli (2001). An energy-based methodology for the assessment of seismic demand, *Soil Dynam. Earthq. Eng.* **21**, 113–137.
- Dindar, A.A., C. Yalçın, E. Yüksel, H. Özkaynak, and O. Büyüköztürk (2015). Development of earthquake energy demand spectra, *Earthq. Spectra* **31**, no. 3, 1667–1689.
- Erberik, A., and H. Sucuoğlu (2004). Seismic energy dissipation in deteriorating systems through low-cycle fatigue, *Earthq. Eng. Struct. Dynam.* **33**, no. 1, 49–67.
- Gong, M. S., and L. L. Xie (2005). Study on comparison between absolute and relative input energy spectra and effects of ductility factor, *Acta Seismol. Sinica* **18**, no. 6, 717–726.
- Housner, G. (1956). Limit design of structures to resist earthquakes, *Proc. of the 1st World Conf. on Earthquake Engineering*, Berkeley, California, June 1956.
- Idriss, I. M., and J. I. Sun (1992). *SHAKE91: A Computer Program for Conducting Equivalent Linear Seismic Response Analyses of Horizontally Layered Soil Deposits, User's Guide*, University of California, Davis.
- Japanese Seismic Design Code (2000). *Technical Standard for Structural Calculation of Response and Limit Strength of Buildings, Notification No.1457–2000*, Ministry of Land, Infrastructure and Transport, Tokyo (in Japanese).
- Kawase, H. (2003). Site effects on strong ground motions, in *International Handbook of Earthquake and Engineering Seismology, Part B*, W. H. K. Lee and H. Kanamori (Editors), Academic Press, London, 1013–1030.
- Kokusho, T. (2017). *Innovative Earthquake Soil Dynamics*, CRC Press, Taylor and Francis Group, London, 45–47.
- Kunnath, S. K., and Y. H. Chai (2004). Cumulative damage-based inelastic cyclic demand spectrum, *Earthq. Eng. Struct. Dynam.* **33**, 499–520.
- Kuwamura, H., and T. V. Galambos (1989). Earthquake load for structural reliability, *J. Struct. Eng.* **115**, 1446–1462.
- Kuwamura, H., Y. Kirino, and H. Akiyama (1994). Prediction of earthquake energy input from smoothed Fourier amplitude spectrum, *Earthq. Eng. Struct. Dynam.* **23**, 1125–1137.
- López-Almansa, F., A. U. Yazgan, and A. Benavent-Climent (2013). Design energy input spectra for high seismicity regions based on Turkish registers, *Bull. Earthq. Eng.* **11**, 885–912.
- Mezgebo, M. G., and E.M. Lui (2016). Hysteresis and soil site dependent input and hysteretic energy spectra for far-source ground motions, *Adv. Civil Eng.* 1,548,319, doi: [10.1155/2016/1548319](https://doi.org/10.1155/2016/1548319).
- Nakano, K., and H. Kawase (2019). Source parameters and site amplifications estimated by generalized inversion technique: Focusing on the 2018 Hokkaido Iburi-Tobu earthquake, *Earth Planets Space* **71**, 66.
- National Earthquake Hazards Reduction Program (NEHRP) (2000). *Recommended Provisions for Seismic Regulations for New Buildings and Other Structures*, Federal Emergency Management Agency, Washington, D.C.
- National Research Institute for Earth Science and Disaster Resilience (NIED) (2019). Strong-motion Seismograph Networks (K-NET, KIK-net), doi: [10.17598/NIED.0004](https://doi.org/10.17598/NIED.0004).
- Okada, Y., K. Kasahara, S. Hori, K. Obara, S. Sekiguchi, H. Fujiwara, and A. Yamamoto (2004). Recent progress of seismic observation networks in Japan—Hi-net, F-net, K-NET and KiK-net-, *Earth Planets Space* **56**, xv–xxviii.
- Ordaz, M., B. Huerta, and E. Reinoso (2003). Exact computation of input-energy spectra from Fourier amplitude spectra, *Earthq. Eng. Struct. Dynam.* **32**, 597–605.

- Riddell, R., and J. E. Garcia (2001). Hysteretic energy spectrum and damage control, *Earthq. Eng. Struct. Dynam.* **30**, 1791–1816.
- Vahdani, R., M. Gerami, and M. A. Vaseghi-Nia (2019). The spectra of relative input energy per unit mass of structure for Iranian earthquakes, *Int. J. Civil Eng.* **17**, 1183–1199.
- Wang, X., and E.M. Rathje (2016). Influence of peak factors on site amplification from random vibration theory-based site-response analysis, *Bull. Seismol. Soc. Am.* **106**, 1733–1746.
- Zahrah, T. F., and W. J. Hall (1984). Earthquake energy absorption in SDOF structures, *J. Struct. Eng.* **110**, 1757–1772.
- Zhang, H. Z., and Y. G. Zhao (2018). A simple approach for estimating the first resonance peak of layered soil profiles, *J. Earthq. Tsunami* **12**, no. 3, 1,850,005.
- Zhang, H. Z., and Y. G. Zhao (2020). Damping modification factor based on random vibration theory using a source-based ground-motion model, *Soil Dynam. Earthq. Eng.* **136**, 106,225.
- Zhang, H. Z., and Y. G. Zhao (2021a). Investigation of relationship between the response and Fourier spectral ratios based on statistical analyses of strong motion records, *J. Earthq. Tsunami* **15**, no. 2, 2,150,008.
- Zhang, H. Z., and Y. G. Zhao (2021b). Effects of earthquake magnitude, distance, and site conditions on spectral and pseudospectral velocity relationship, *Bull. Seismol. Soc. Am.* **111**, no. 6, 3160–3174.
- Zhang, H. Z., and Y. G. Zhao (2021c). Damping modification factor of acceleration response spectrum considering seismological effects, *J. Earthq. Eng.* doi: [10.1080/13632469.2021.1991521](https://doi.org/10.1080/13632469.2021.1991521).
- Zhang, H. Z., and Y. G. Zhao (2021d). Analytical model for response spectral ratio considering the effect of earthquake scenarios, *Bull. Earthq. Eng.* **19**, no. 1, 5285–5305.
- Zhang, H. Z., Y. G. Zhao, F. W. Ge, Y. C. Fang, and T. Ochiai (2023). Estimation of input energy spectrum from pseudo-velocity response spectrum incorporating the influences of magnitude, distance, and site conditions, *Eng. Struct.* **274**, 115,165.
-
- Manuscript received 25 July 2022
Published online 7 March 2023